Chapter VI
Sm and Sr Co-Doped Ceria and its Nanocomposites

This chapter contains two sections. Section 1 deals with the study on Sm and Sr co-doped ceria. The composition which shows the highest electrical conductivity in this system has been chosen for the nanocomposites. Effect of carbonates [$(Li_{0.52}Na_{0.48})_2CO_3$] content on the thermal behavior, phases, structure, morphology and electrical properties of Sm and Sr co-doped ceria has been discussed in the section 2.

6.1 Sm and Sr Co-Doped Ceria

6.1.1 Introduction

Solid oxide fuel cells (SOFCs) are the energy converters. These convert chemical energy into electrical energy. Solid oxide electrolytes with high ionic conductivity at low temperatures are the key components for SOFCs. So far, yttria-stabilized zirconia (YSZ) has been used as a solid electrolyte due to its high ionic conductivity and stability at high temperature. Sealing of SOFC units using YSZ requires high temperature. This puts constraint of using expensive materials for various components of the cells. To be cost effective, it is necessary therefore, to develop solid electrolytes having high ionic conductivity at low temperatures (500-700 ^oC). Gd doped ceria (GDC) and Sm doped ceria (SDC) are considered to be the most promising low temperature solid electrolytes for such applications because of their high oxide ion conductivity in the temperature range 500-700 ^oC [Minh et al. (1995)]. But both Gd and Sm are very costly. In order to reduce the cost and to identify new systems, a co-doping approach has been introduced [Omar et al. (2006); Sha et al. (2007); Herle et al. (1999)].

Readily available alkaline earth oxides are more cost effective than the rare earth oxides. The most distinguished feature of using alkaline earth ions as co-dopants is the scavenging of siliceous impurities present at grain boundaries thereby,

increasing the grain boundaries conductivity. Previous results have shown that MgO, CaO, SrO and BaO are effective grain boundaries scavengers for Gd-doped ceria (GDC) [Cho et al. (2009); Cho et al. (2008); Park et al. (2009); Cho et al. (2007)]. Cioatera et al. [Ciotera et al. (2009)] studied the effect of strontium addition on the properties of europium-doped ceria. They found a significant diminution of grain boundaries resistance after simultaneous substitution of europium and strontium in ceria. Some other examples of strontium co-doped electrolytes are $Ce_{0.80-x}Sm_{0.20}Sr_xO_{2-\delta}$ [Tsung et al. (2007)], (1-x)SDC-xSr [Zheng et al. (2011)], $Ce_{0.80-x}Gd_{0.20}Sr_xO_{2-\delta}$ [Ramesh et al. (2009)] and $Ce_{0.80}Y_{0.20-x}Sr_xO_{2-\delta}$ [Zheng et al. (2009)]. In all these compositions studied the concentration of oxygen vacancies changes with concentration (x) of Sr^{2+}.

$Ce_{1-x-y}Sm_xSr_yO_{1.90}$ compositions have been presented in the present chapter because Sm has been proved to be a very good dopant that produces the highest conductivity and also decreases the reducibility of ceria [Mogensen et al. (2000)]. Nanocrystalline powders in the system, $Ce_{1-x-y}Sm_xSr_yO_{1.90}$ [(x=0.20, y=0.0; SDC), (x=0.16, y=0.02; 2SrSDC), (x=0.12, y=0.04; 4SrSDC) and (x=0.08, y=0.06; 6SrSDC)] having the same molar concentration of oxygen vacancies have been prepared and characterized. The purpose of the study is to investigate the effect of co-doping of Sr^{2+} only on the ionic conductivity keeping the total number of oxygen vacancies constant.

6.1.2 Results and Discussion

(a) Crystal structure and phases

Powder X-ray diffraction patterns of all the calcined and sintered samples are recorded. XRD patterns show the formation of a single phase solid solution having cubic fluorite structure similar to that of CeO_2. XRD patterns for the calcined samples are similar to those obtained after sintering except that the diffraction lines become sharper after sintering. This is due to grain growth occurring during sintering. Diffraction patterns are indexed on the basis of structure of CeO_2 using JCPDS file no. 43-1002. Average crystallite size, D, of the calcined powders, calculated by Scherrer's formula from X-ray line broadening is in the range 20-27 nm (Table.6.1).

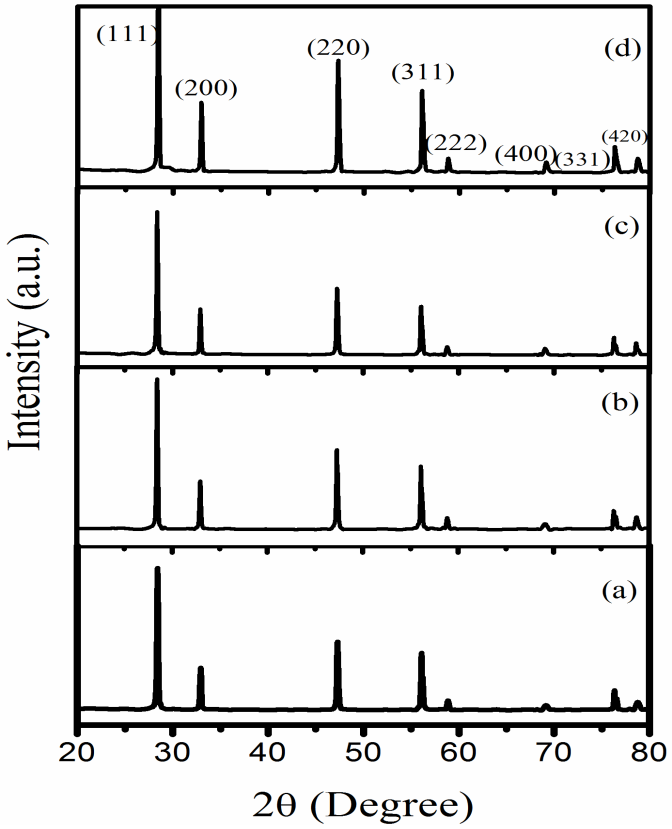

Fig. 6.1 Powder XRD patterns of the sintered samples in the system $Ce_{1-x-y}Sm_xSr_yO_{1.90}$ system with (a) SDC (b) 2SrSDC (c) 4SrSDC and (d) 6SrSDC

Powder XRD patterns of all the sintered samples are shown in Fig. 6.1. It is noted that the 2θ values of co-doped ceria shift slightly toward higher angles with increasing Sr content. Samples sintered at 1350 °C have density more than 95% of the theoretical values (Table.6.1). Lattice parameter is determined using "Unit Cell" software. Lattice parameter increases from 5.4019+/-0.0016 Á [Singh et al. (2011)] to 5.4354+/-0.0009 Á on addition of 20 mol% Sm to CeO_2 because ionic radius of Sm^{3+} (1.079 Á) is larger than that of Ce^{4+} (0.97 Á) [Shannon (1976)]. Lattice parameter of the system $Ce_{1-x-y}Sm_xSr_yO_{1.90}$ decreases with increasing the Sr content as shown in Fig. 6.2 because total dopant content decreases to maintain the molar concentration of oxygen vacancies constant in all the samples.

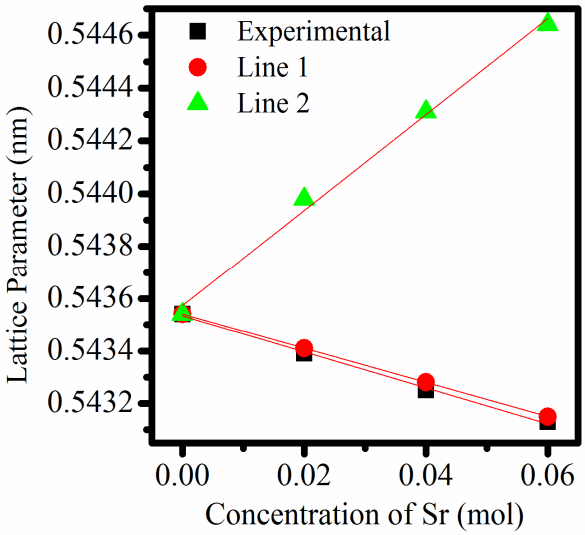

Fig. 6.2 Variation of lattice parameter with Sr content in the system $Ce_{1-x-y}Sm_xSr_yO_{1.90}$

The radius of oxygen vacancies formed by trivalent ($r_{V_{O_t}^{\cdot\cdot}}$) and divalent dopant cations ($r_{V_{O_d}^{\cdot\cdot}}$) determined using hard sphere model has been found to be 1.149 Å and 0.9498 Å respectively in the system $Ce_{1-x-y}Sm_xSr_yO_{1.90}$ [Hong et al. (1995)]. Theoretical values of lattice parameter determined using Eq^n (6.1) are plotted in Fig. 6.2. Line 1 shows the data when the values of $r_{V_{O_t}^{\cdot\cdot}}$ and $r_{V_{O_d}^{\cdot\cdot}}$ are different. Line 2 shows the data when the average radius of oxygen vacancies (1.16 Å) is used.

$$a = \frac{4}{\sqrt{3}}\left[xr_{Sm} + yr_{Sr} + (1-x-y)r_{Ce} + \left(\frac{1.9}{2}\right)r_o + \left(\frac{x}{4}r_{V_{O_t}^{\cdot\cdot}} + 0.5yr_{V_{O_d}^{\cdot\cdot}}\right)\right] \quad (6.1)$$

where r_{Ce}, r_{Sr}, r_{Sm}, $r_{V_O^{\cdot\cdot}}$ and r_O are radii of Ce^{4+}, Sr^{2+}, Sm^{3+}, oxygen vacancy and oxygen ion respectively. It is noted from Fig.6.2 that the experimental values are close to the line 1. It can be concluded therefore that radius of oxygen vacancies formed by trivalent and divalent cations are different in the system $Ce_{1-x-y}Sm_xSr_yO_{1.90}$. Value of $r_{V_{O_t}^{\cdot\cdot}}$ is more than that of $r_{V_{O_d}^{\cdot\cdot}}$. This provides more wide conducting channel for transport of the O^{2-} ions.

Table. 6.1 Crystallite size (calcined powders), lattice parameter and % theoretical density of all the compositions in the system $Ce_{1-x-y}Sm_xSr_yO_{1.90}$

S. No.	x & y	Sample code	Lattice parameter (Å)	Crystallite size (nm)	%TD
1.	0.20 & 0.0	SDC	5.4354+/-0.0009	20	97.0
2.	0.16 & 0.02	2SrSDC	5.4339+/-0.0006	25	98.0
3.	0.12 & 0.04	4SrSDC	5.4325+/-0.0007	22	95.0
4.	0.08 & 0.06	6SrSDC	5.4313+/-0.0005	27	95.0

(b) Microstructure

Figs. 6.3 (a)-(d) show the SEM micrographs of all the sintered samples. Micrographs of the sintered samples show a dense structure and well defined grains separated by the grain boundaries. All the samples show grains of varying size and have faceted grain boundaries. The average grain size for the samples SDC, 2SrSDC, 4SrSDC and 6SrSDC is found to be 1.0, 3.0, 2.4 and 2.3 μm respectively. Figs. 6.4 and 6.5 show the EDS spectrum of SDC and 2SrSDC at three different points in the specimen respectively. It can be seen from these spectra that the grain, grain boundary and triple point have the same constituent elements but a second phase Si is present at the grain boundary. In the case of composition, 2SrSDC, however, Si is present at the triple point and there is no Si present at the grain boundary. It is concluded that Sr reacts with silica to form some silicate phase which segregates at the triple point. This leaves clean grain boundaries and increases grain to grain contact area. The composition and morphology of the formed silicate phases needs to be determined using STEM equipped with EELS and EDXM [Gerhardt et al. (1986)]. In the spectra an extra element Au is also present. It comes from the gold coating on the samples.

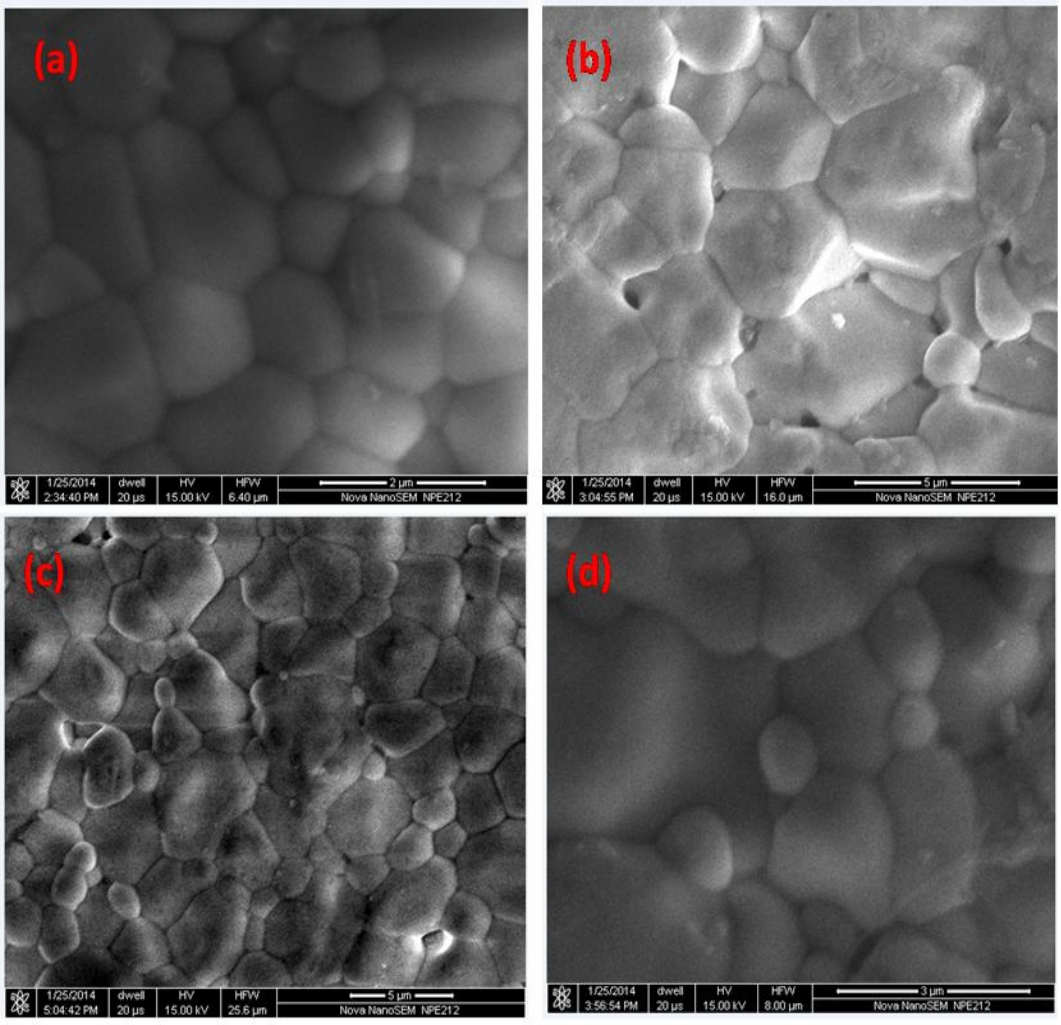

Fig. 6.3 SEM micrographs of the sintered samples of compositions (a) SDC (b) 2SrSDC(c) 4SrSDC and (d) 6SrSDC

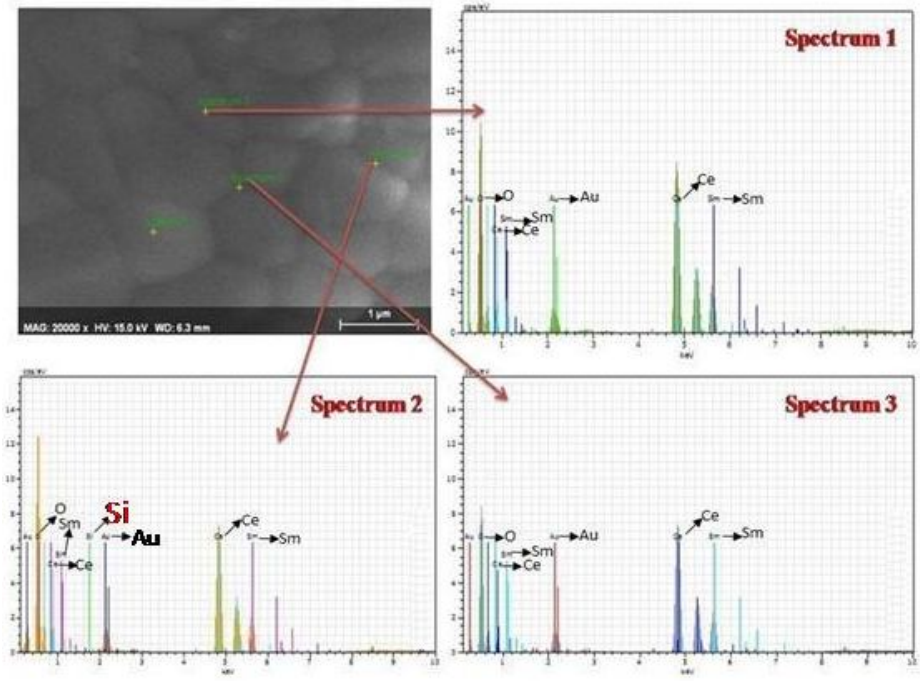

Fig. 6.4 EDS spectrum of the composition SDC at three spectrum points

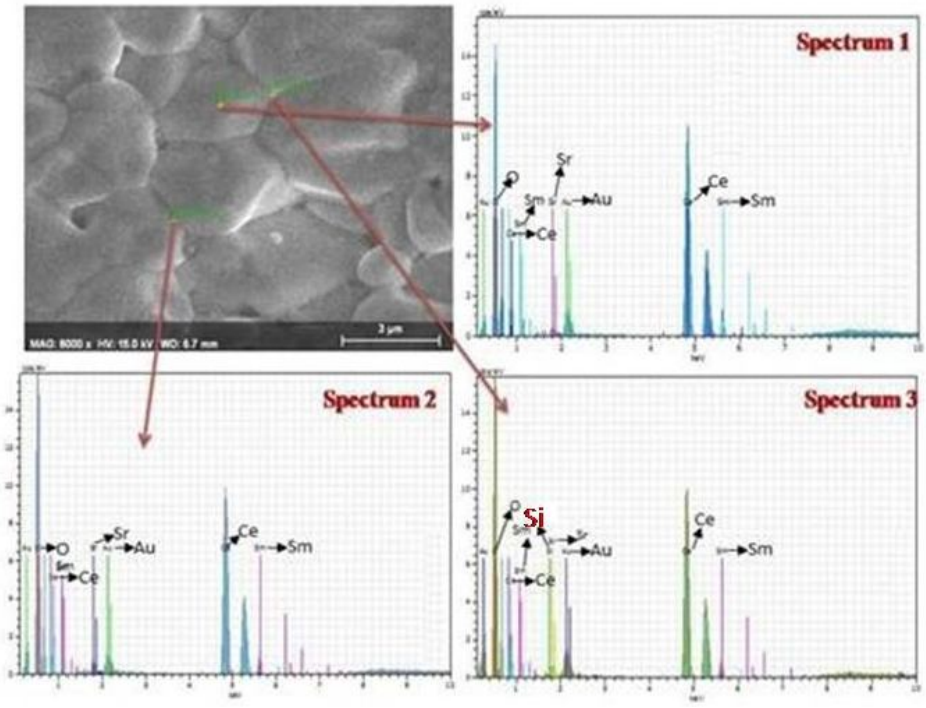

Fig. 6.5 EDS spectrum of the composition 2SrSDC at three different points

(c) Electrical conductivity

Figs. 6.6 - 6.9 show the complex plane impedance plots of all the compositions in the system $Ce_{1-x-y}Sm_xSr_yO_{1.90}$. In the temperature range 200-275 ºC, three arcs have been observed for the composition, SDC. A high frequency arc passing from the origin is ascribed to the contribution of the grains, intermediate frequency arc is ascribed to the contribution of the grain boundaries and a tail in the low frequency range corresponds to the electrode/electrolyte contribution to the total resistance. Due to increase of relaxation frequency with the temperature, the grains and grain boundaries arcs disappear above 275 and 525 ºC respectively. Capacitance of the grains and grain boundaries arcs determined using the relation $2\pi f_{max}RC = 1$ are in the pF (10^{-10}-10^{-12}) and nF (10^{-7}-10^{-9}) ranges respectively [Hodge et al. (1976)].

Figs. 6.7, 6.8 and 6.9 show the impedance plots of the compositions 2SrSDC, 4SrSDC and 6SrSDC respectively at different temperatures. Three arcs have been found in the range 200-275 ºC. The arcs of grains and grain boundaries disappear above 275 and 400 ºC respectively. It is seen from Fig. 6.7 that the arc of the grain boundaries is small as compared to that in singly Sm doped ceria. Above 425 ºC, only the arc due to electrode/electrolyte interface is observed.

The impedance plots are fitted to an equivalent circuit as shown in the Figs. 6.6-6.9. The sum of resistance of the grains and the grain boundaries is equal to the total resistance of the sample. Therefore, only arcs of the grains and the grain boundaries are fitted. The arc due to electrode is not fitted. The intercept on higher frequency side of the electrode arc on real Z' axis has been taken as total resistance of the sample when the arcs due to grains and grain boundaries disappear.

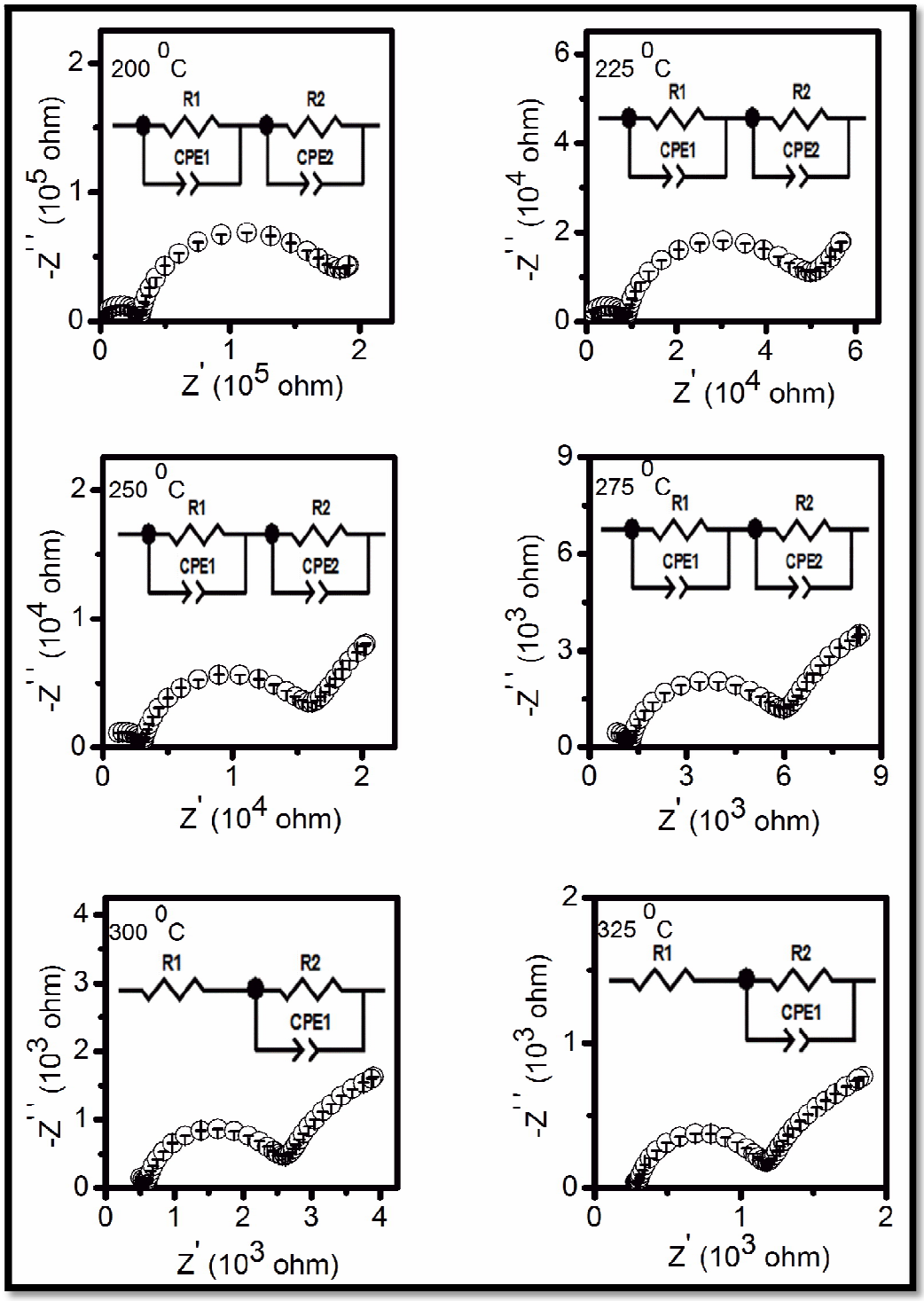

Fig. 6.6 Complex plane impedance plots of the composition SDC at different temperatures

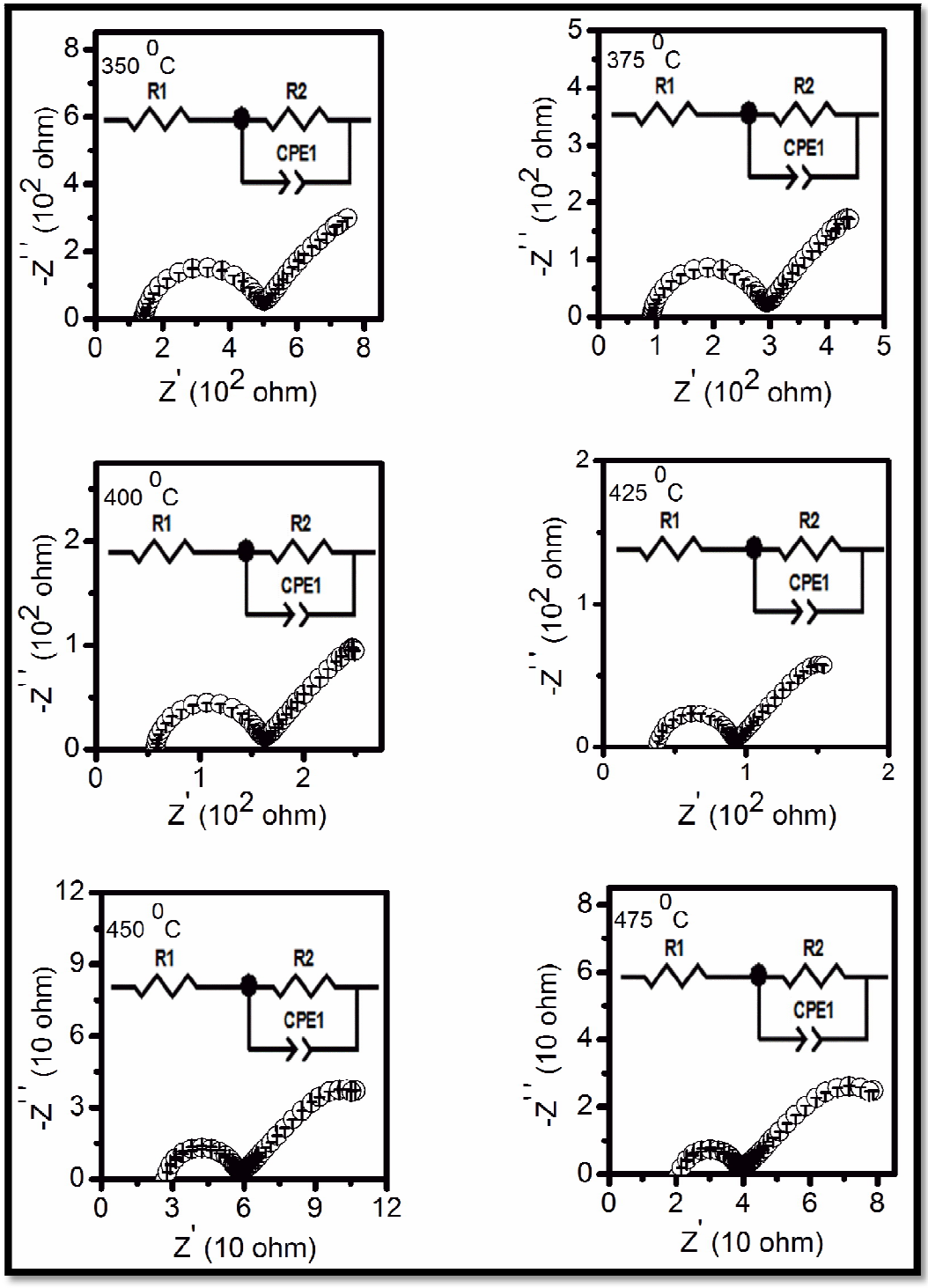

Fig. 6.6 Complex plane impedance plots of composition SDC at different temperatures

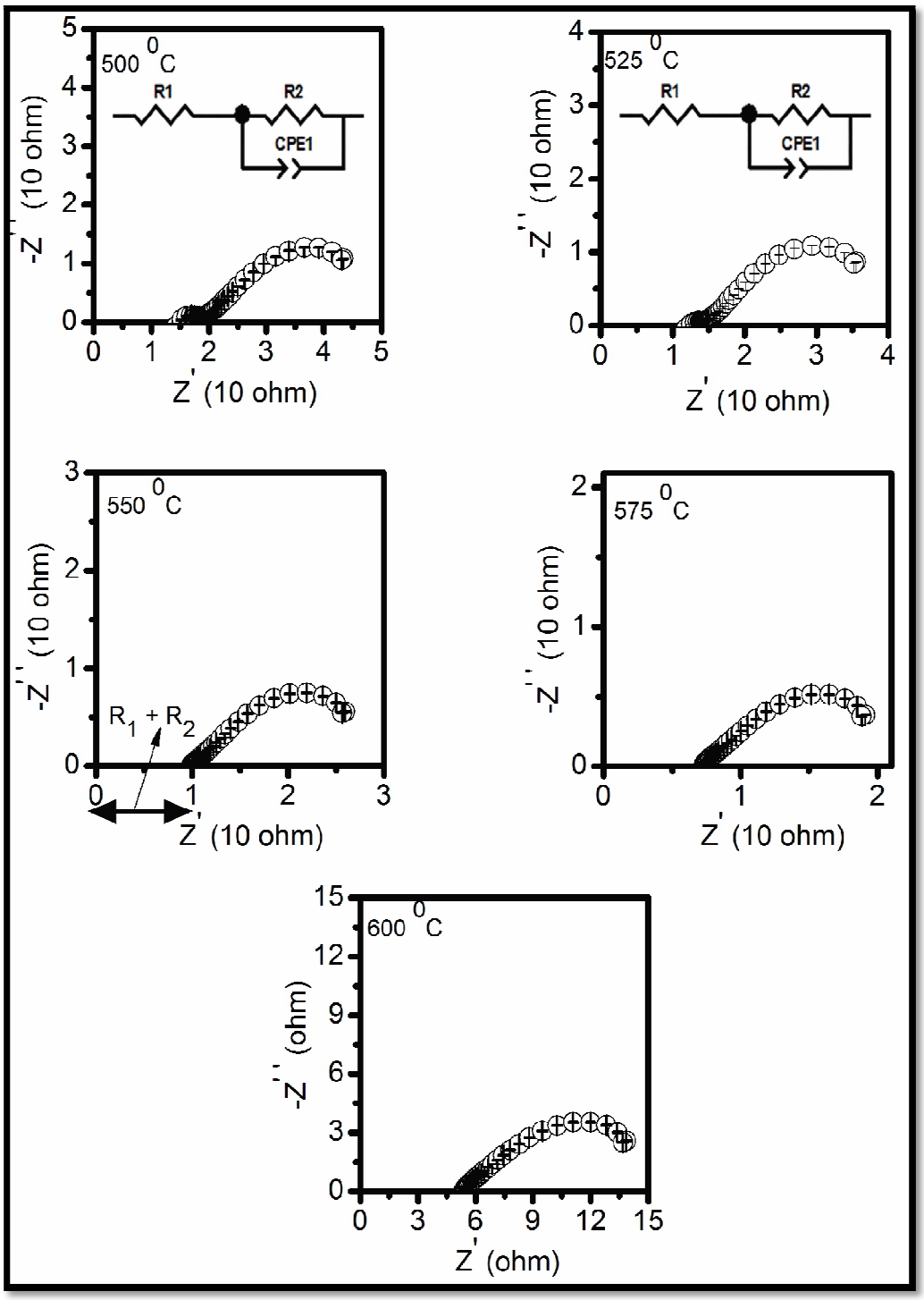

Fig. 6.6 Complex plane impedance plots of composition SDC at different temperatures

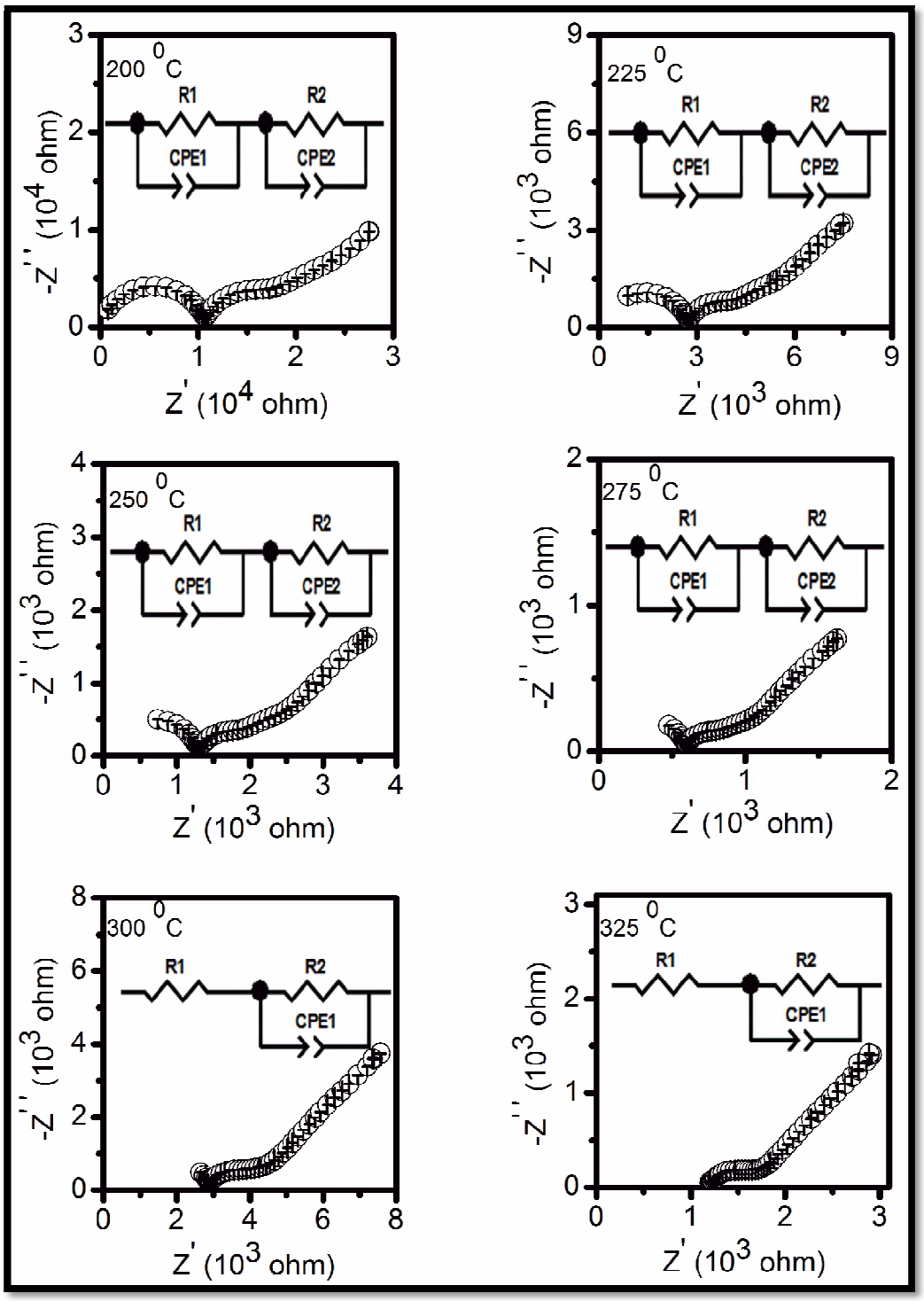

Fig. 6.7 Complex plane impedance plots of the composition 2SrSDC at different temperatures

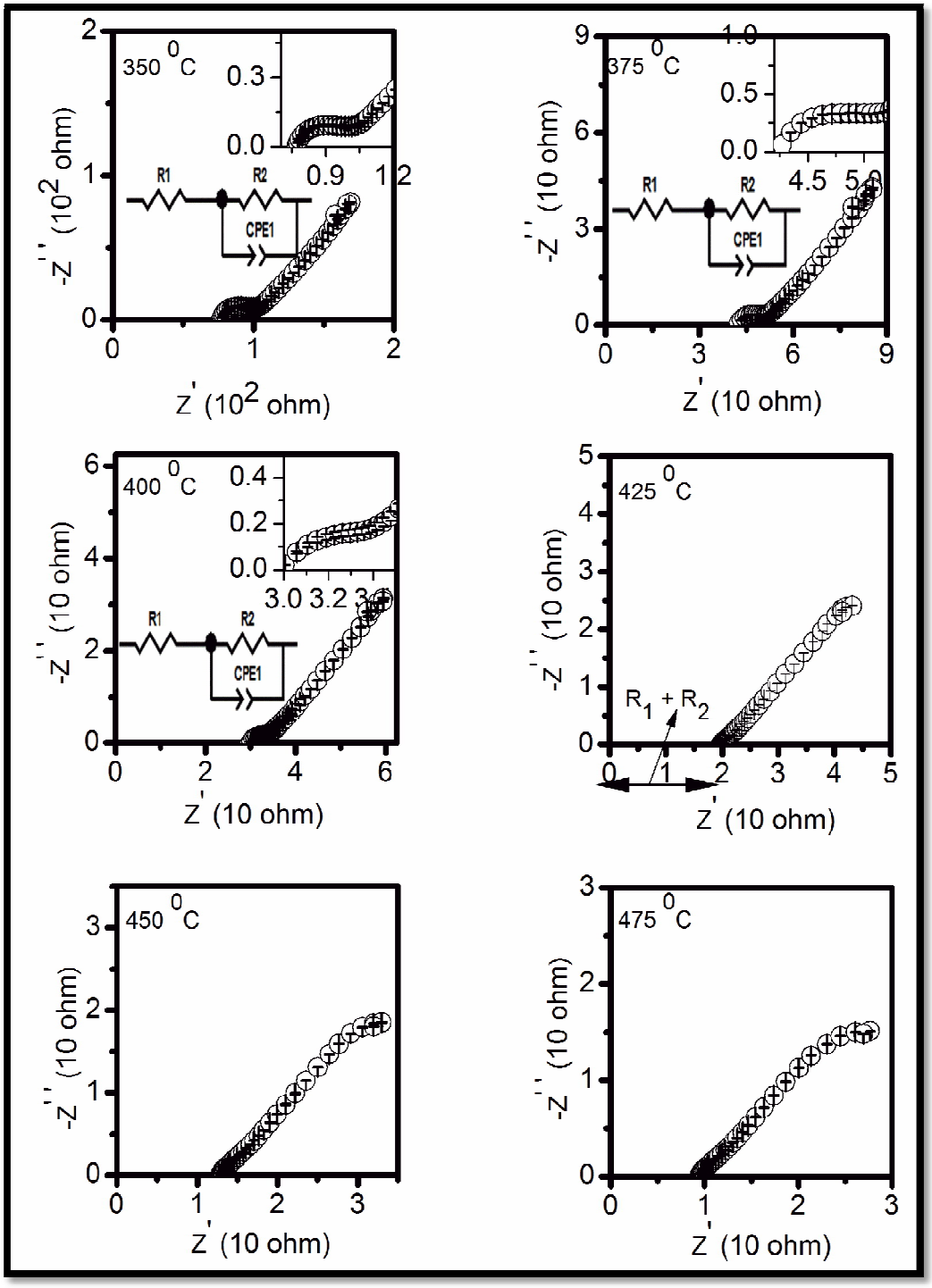

Fig. 6.7 Complex plane impedance plots of the composition 2SrSDC at different temperatures

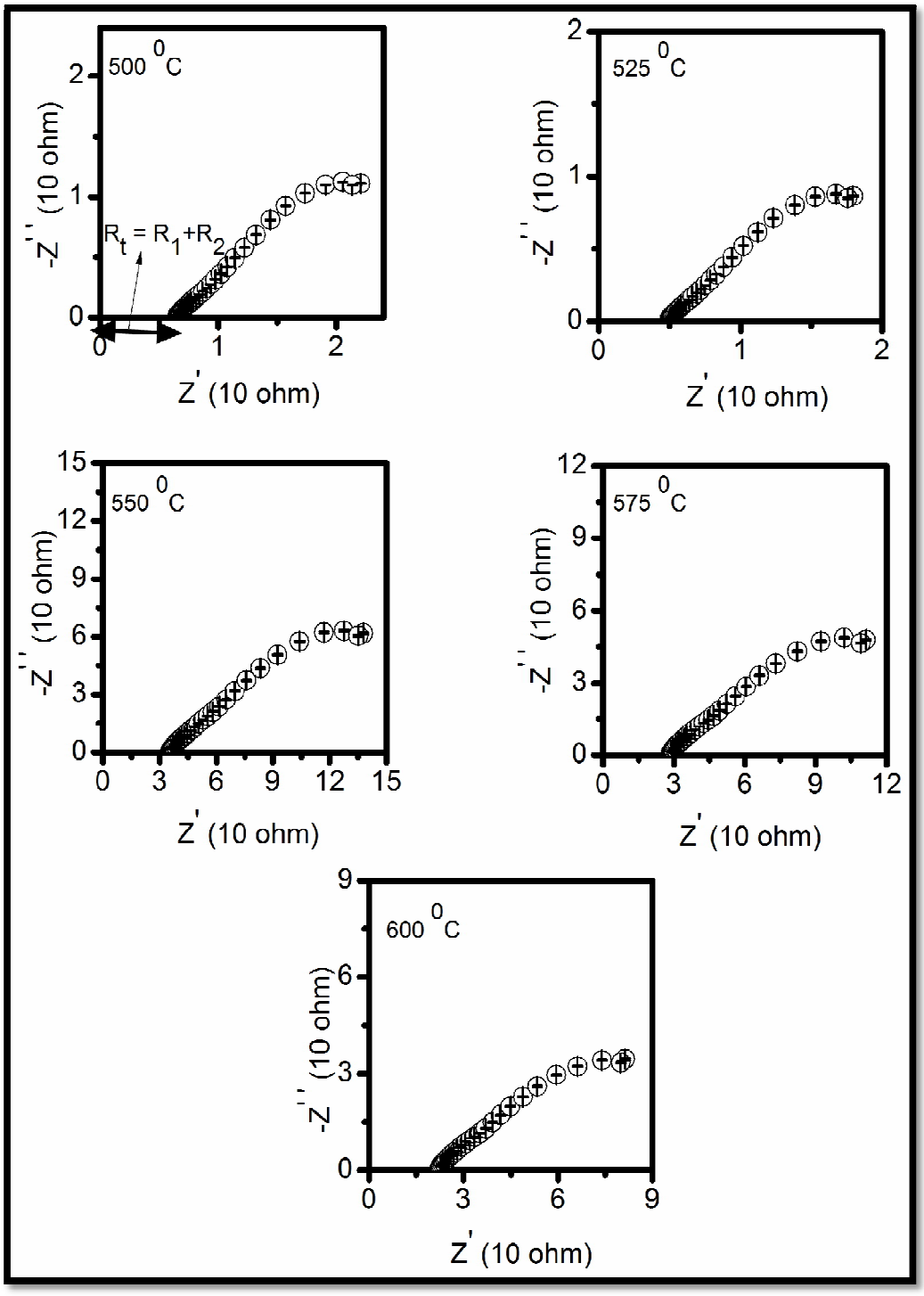

Fig. 6.7 Complex plane impedance plots of the composition 2SrSDC at different temperatures

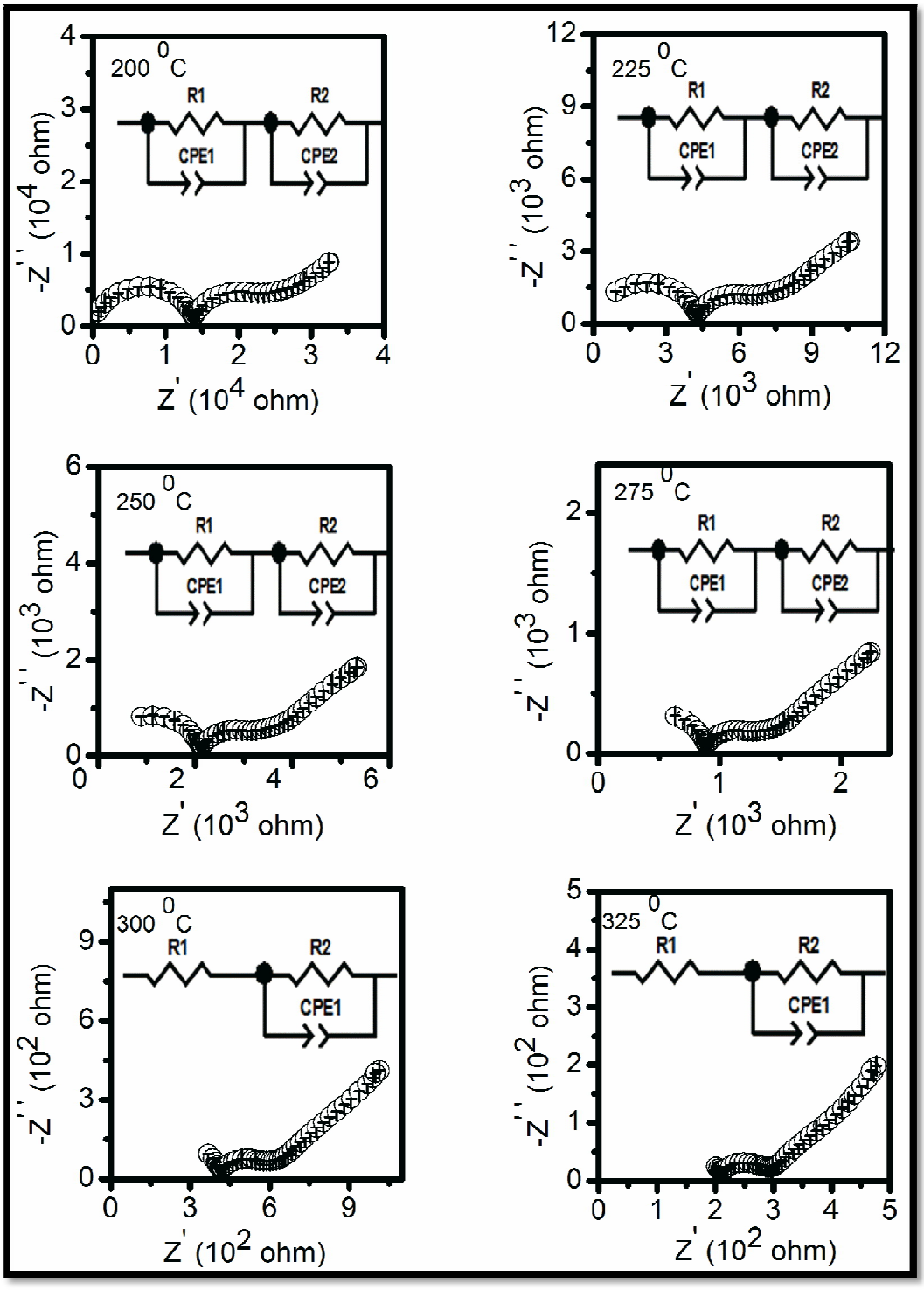

Fig. 6.8 Complex plane impedance plots of the composition 4SrSDC at different temperatures

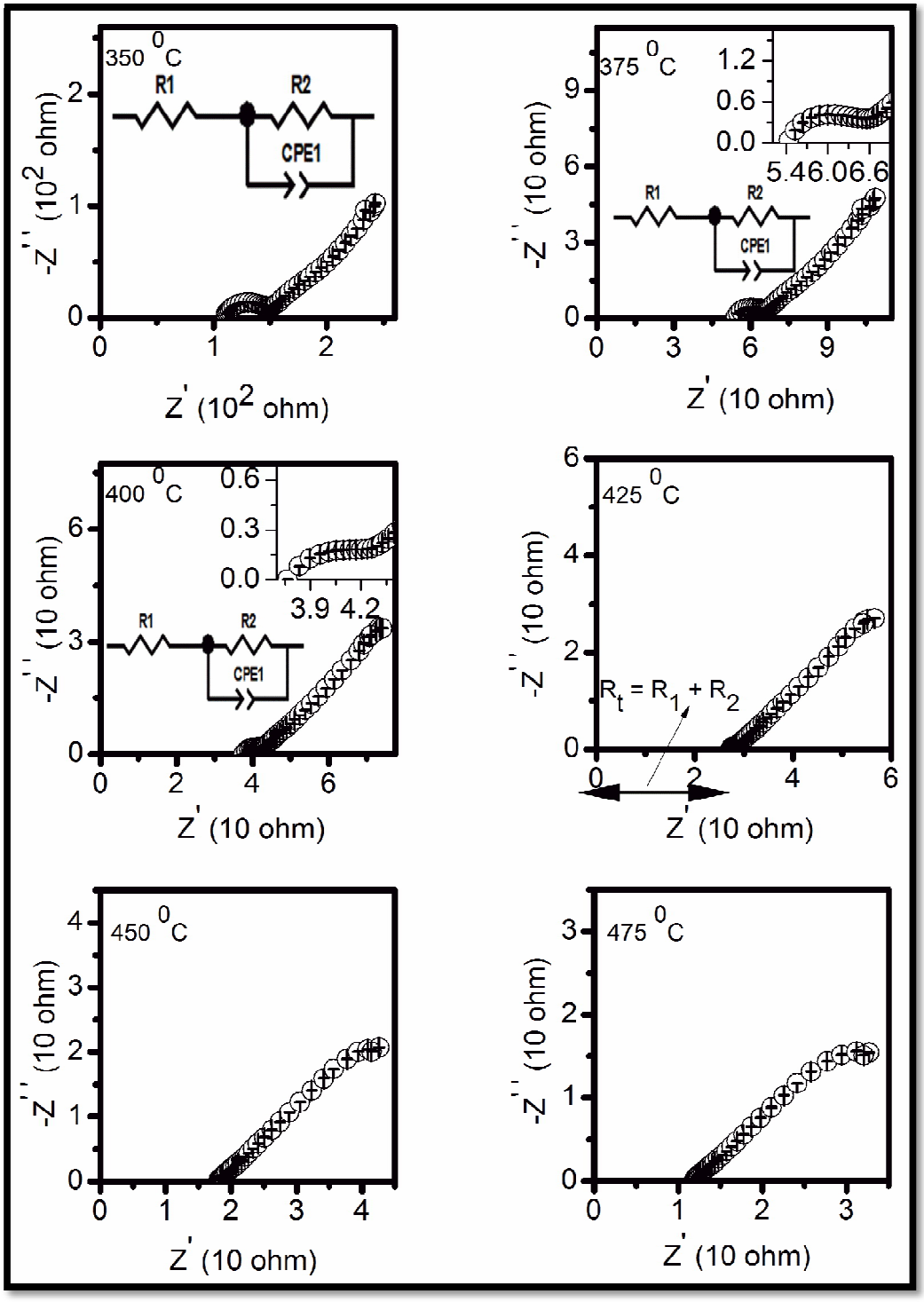

Fig. 6.8 Complex plane impedance plots of the composition 4SrSDC at different temperatures

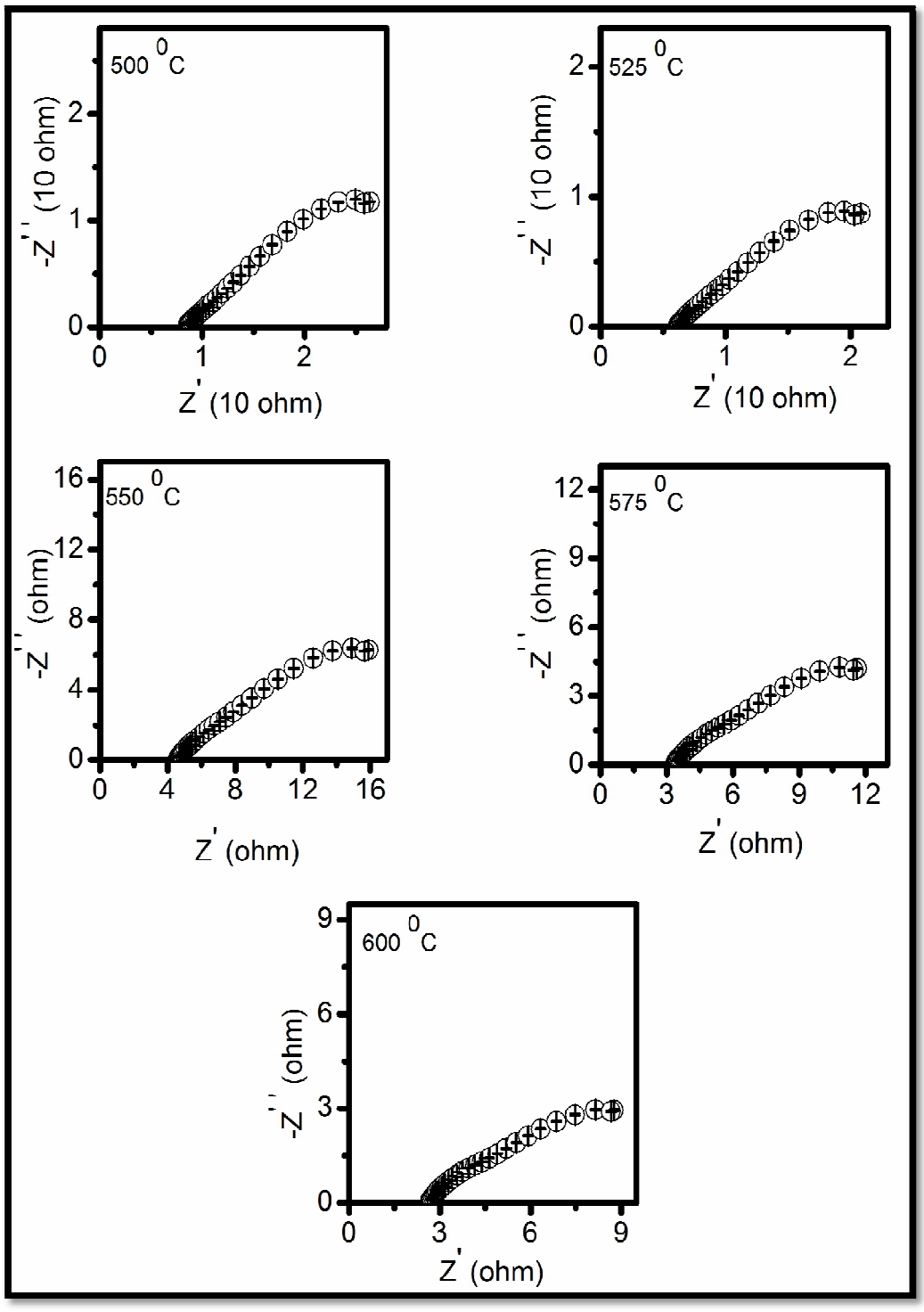

Fig. 6.8 Complex plane impedance plots of the composition 4SrSDC at different temperatures

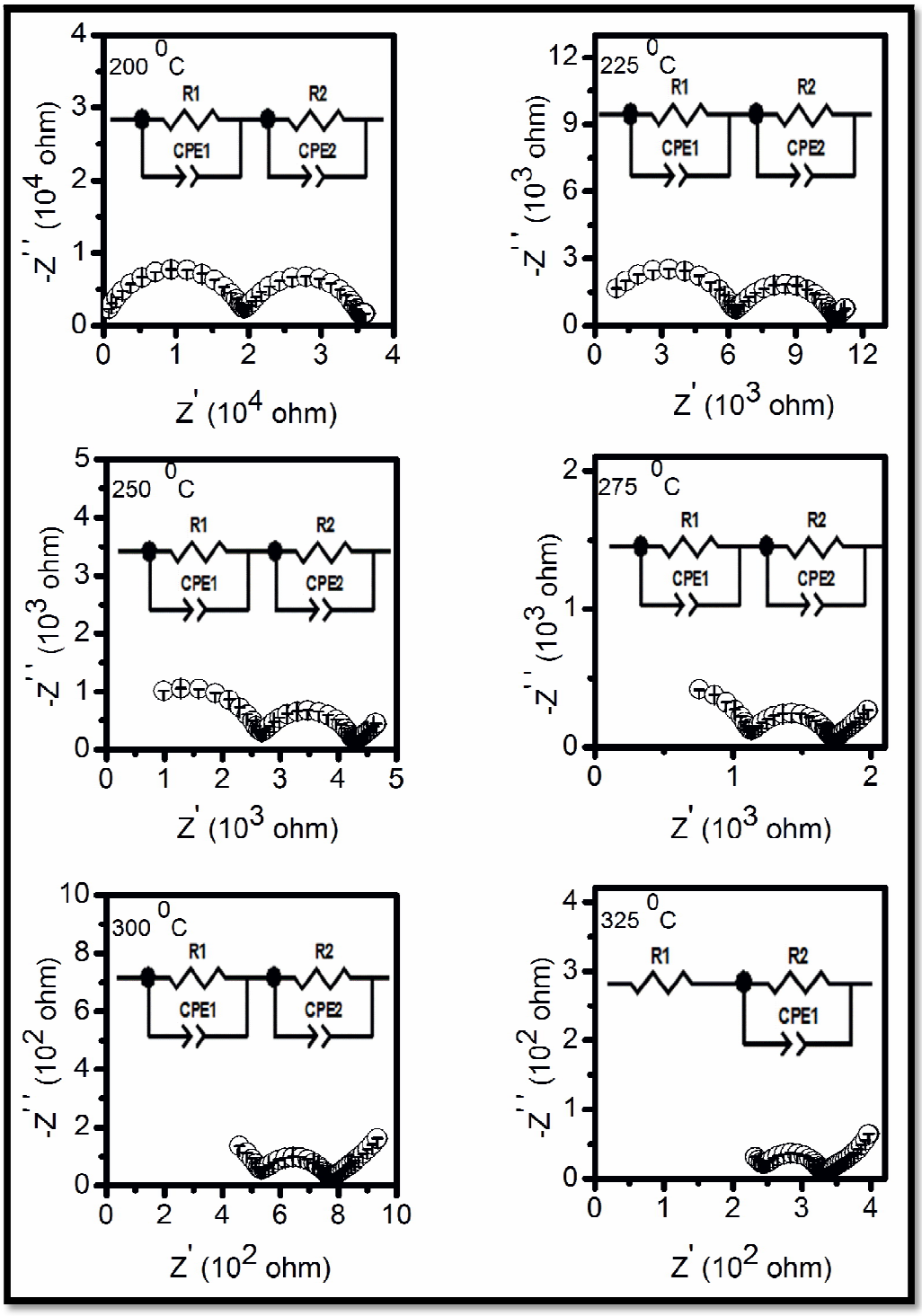

Fig. 6.9 Complex plane impedance plots of the composition 6SrSDC at different temperatures

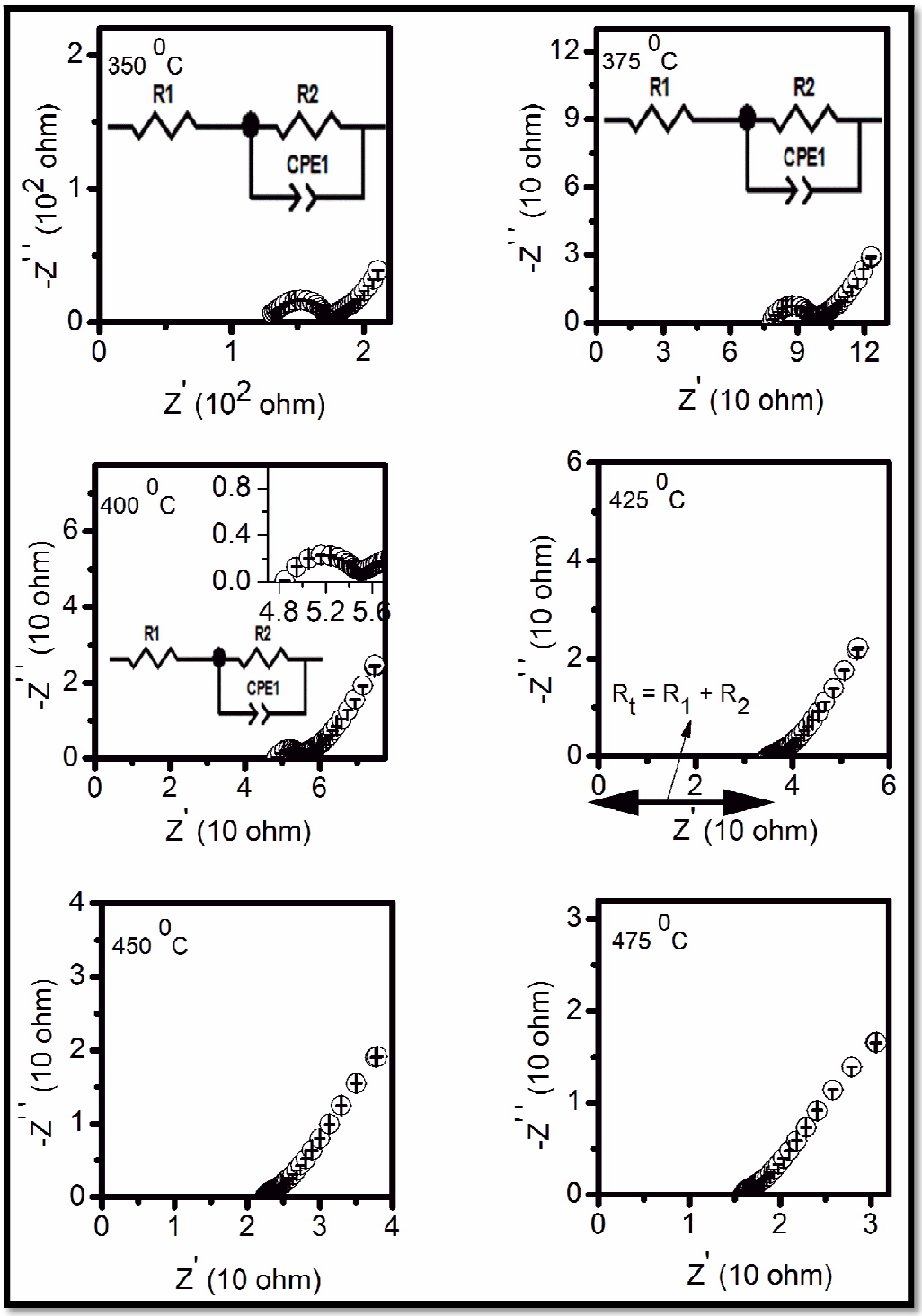

Fig. 6.9 Complex plane impedance plots of the composition 6SrSDC at different temperatures

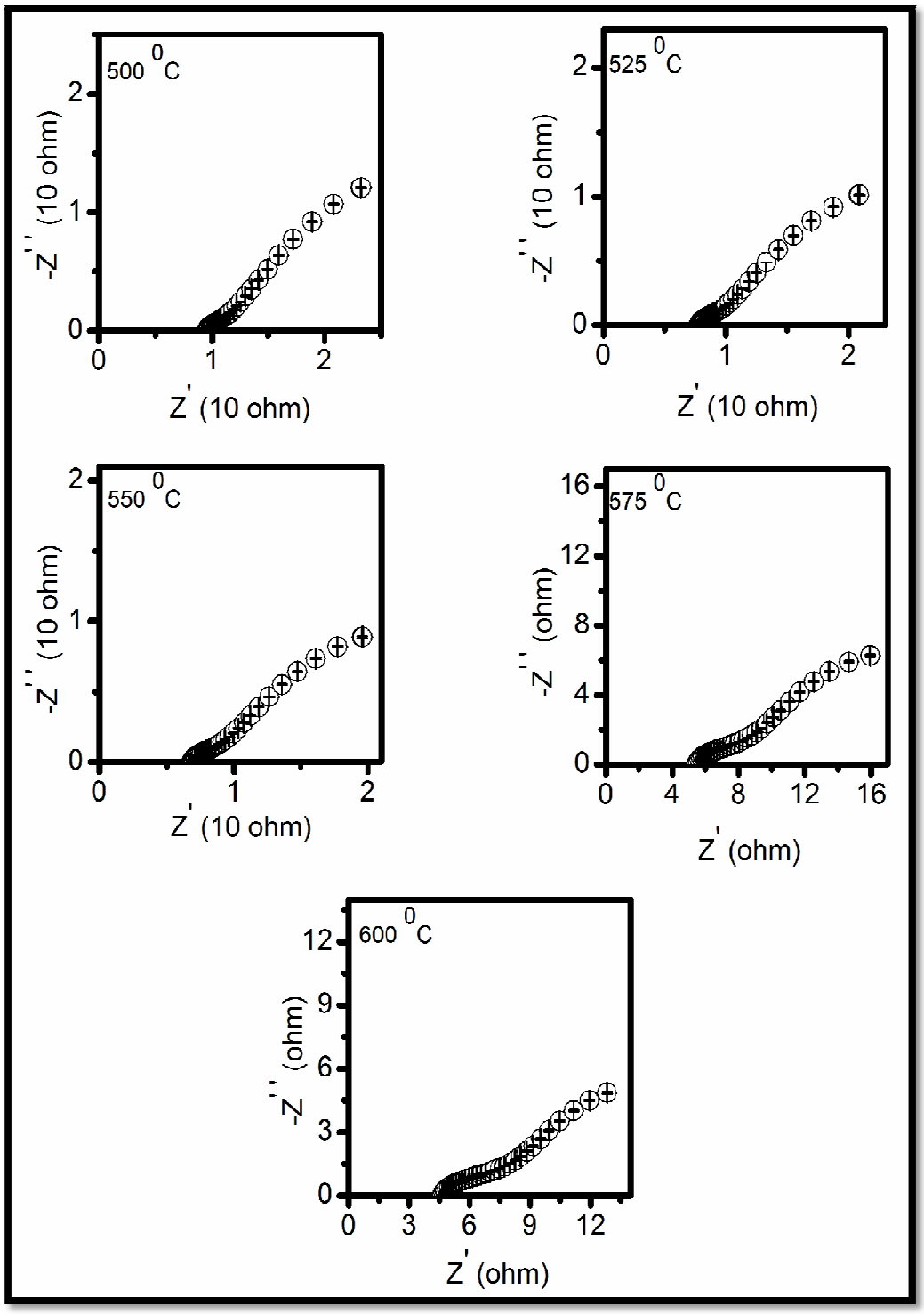

Fig. 6.9 Complex plane impedance plots of the composition 6SrSDC at different temperatures

Fig. 6.10 shows Arrhenius plots for the bulk conductivity (σ_g), grain boundaries conductivity (σ^*_{gb}) and the total conductivity (σ_t) of the system $Ce_{1-x-y}Sm_xSr_yO_{1.90}$. It is seen from Fig.6.10 that the bulk conductivity of co-doped samples is higher than that of SDC. Composition, 2SrSDC shows the highest bulk ionic conductivity of all the compositions. For higher concentration of Sr^{2+} i.e. for x > 0.02, the bulk conductivity decreases. Activation energy of conduction for the bulk conductivity is determined by fitting the conductivity data points to Arrhenius equation and is given in Table. 6.2. Composition 2SrSDC has the leastt activation energy of conduction among all the samples.

σ^*_{gb}, is also higher for the co-doped samples. This may be due to scavenging effect of Sr. Blocking factor, α_{gb} for all the compositions is given in Table. 6.3. α_{gb} for the sample, 2SrSDC is 0.19 while it is 0.66 for SDC. Similar to the previously reported results in zirconia and ceria ceramics [Guo et al. (2006)] it follows that Sr reacts with Si present at the grain boundaries to produce a different silicate phase which segregates at the triple points. At triple points, the presence of these secondary phases has less effect on the conductivity than a Si phase at the grain boundaries. This is also in conformity with the results of EDS i.e. Si is present at the grain boundary for composition SDC. In the case of composition, 2SrSDC, Si is present at triple point only.

σ^*_{gb} depends on the aspect ratio, $\frac{\delta_{gb}}{d_g}$ i.e. the ratio of the thickness of the grain boundaries to that of average grain size. Samples with higher aspect ratio have high grain boundaries conductivity. Values of aspect ratio of all the compositions are given in Table. 6.3. Composition, 2SrSDC has the highest $\sigma^*_{gb}$with least value of the activation energy of conduction (Table. 6.2).

Activation energy of conduction for the total conductivity is determined using Arrhenius relationship for a thermally activated conduction:

$$\sigma_t = \frac{\sigma_0}{T} \exp - \frac{E_t}{kT} \qquad (6.2)$$

where, E_t is the activation energy of conduction of O^{2-} ions, k is the Boltzmann's constant, T is temperature in Kelvin, and σ_0 is the pre-exponential factor.

It is seen from the Log $\sigma_t T$ vs 1000/T plots that a change in the slope is observed at 500 ^oC which indicates the change of associated defect pairs into dissociated defects.

Table. 6.2 Activation energy of grains (E_g), grain boundaries (E_{gb}) and total (E_t) conductivity of all the compositions in the system $Ce_{1-x-y}Sm_xSr_yO_{1.90}$

S. No.	x & y	Sample code	E_g (eV) (200-400 ^oC)	E_{gb} (eV) (200-400 ^oC)	E_t (eV)	
					(200-500 $^\circ C$)	(500-600 $^\circ C$)
1.	0.20 & 0.0	SDC	0.91	1.04	0.99	0.82
2.	0.16 & 0.02	2SrSDC	0.85	0.99	0.90	0.66
3.	0.12 & 0.04	4SrSDC	0.87	1.08	0.91	0.74
4.	0.08 & 0.06	6SrSDC	0.88	1.08	0.92	0.59

Activation energy at low temperature is the sum of association enthalpy (ΔH_a) of the defect pairs such as $[Sm'_{Ce} - V_O^{\bullet\bullet}]^{\bullet}/[Sr''_{Ce} - V_O^{\bullet\bullet}]^{\times}$ and migration enthalpy (ΔH_m) of oxygen ions. In the low temperature region, oxygen vacancies form associated defect pairs with dopant ions. As the temperature increases, the dissociation of these defect pairs takes place and oxygen vacancies are free to take part in conduction. Arrhenius plots for the total ionic conductivity have been fitted by two straight lines. The association enthalpy obtained [determined by subtracting the activation energy at high temperatures (ΔH_m) from that at low temperatures ($\Delta H_a + \Delta H_m$)] is small in the range 0.17-0.33 eV. These values are similar to the value (ΔH_a = 0.28 eV) obtained by Arachi et al. [Arachi et al. (1999)] in 8 mol% YSZ. Fig. 6.11 illustrates the activation energy of conduction for the grains, grain boundaries and the total measured above and below 500 ^oC as a function of Sr (y) content.

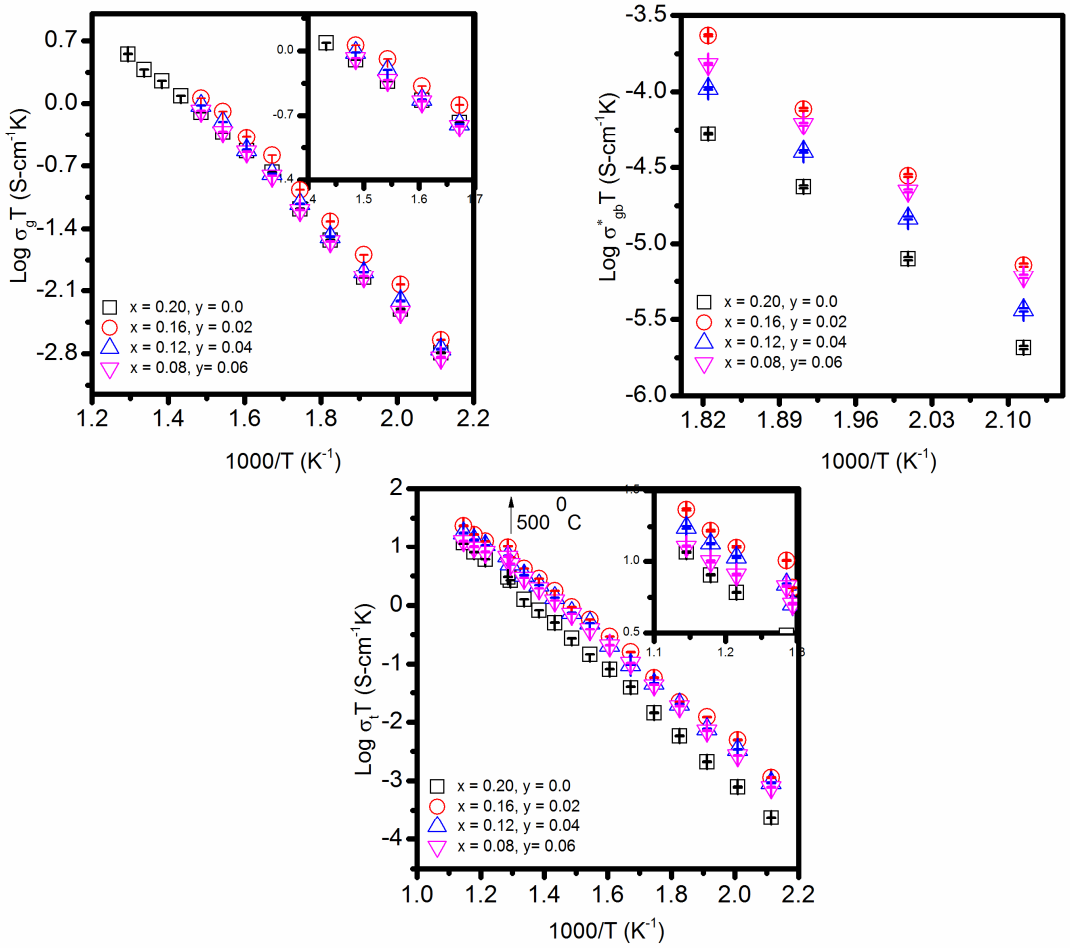

Fig. 6.10 Arrhenius plots for grains, grain boundaries and total conductivity of all the compositions in the system $Ce_{1-x-y}Sm_xSr_yO_{1.90}$

It is seen that the activation energy for the samples change with Sr content exhibiting a minimum for x + y = 0.18 (Table.6.2). The change in activation energy with composition is correlated with the variation in the conductivity. The maximum value of total ionic conductivity corresponds to the minimum activation energy in agreement with the Meyer-Neldel compensation rule [Meyer et al. (1937)]. Values of the total conductivity and configurational entropy of all the samples are given in Table. 6.3. Composition, 2SrSDC shows the highest conductivity 2.67×10^{-2} S/cm at 600 °C with maximum configurational entropy. This value of conductivity is about 50% more than the CeO_2 doped singly with Sm.

It is also more than the highest values reported for 0.94SDC-0.06Sr (~1.13×10^{-2} S/cm) [Zheng et al. (2011)], $Ce_{0.70}Sm_{0.2}Ca_{0.10}O_{2-\delta}$ (2.58×10^{-2} S/cm) [Ramesh et al. (2010)], $Ce_{0.8-x}Sm_{0.10}Mg_{0.10}O_{2-\delta}$ (1.491×10^{-2} S/cm) [Zheng et al. (2009)] and $Ce_{0.8}Sm_{0.10}Y_{0.10}O_{1.9}$ (1.44×10^{-2} S/cm) [Sha et al. (2006)] at 600 °C.

Table. 6.3 Aspect ratio ($\frac{\delta_{gb}}{d_g}$), grain boundary blocking factor (α_{gb}), configurational entropy (S) and total ionic conductivity (σ_t) at 600 ºC of all the compositions in the system $Ce_{1-x-y}Sm_xSr_yO_{1.90}$

S. No.	x & y	Sample code	$\frac{\delta_{gb}}{d_g}$	α_{gb}	σ_t at 600 °C (S/cm)	S (J/mol K)
1.	0.20 & 0.0	SDC	2.20×10^{-3}	0.66	1.33×10^{-2}	4.16
2.	0.16 & 0.02	2SrSDC	3.98×10^{-3}	0.19	2.67×10^{-2}	4.50
3.	0.12 & 0.04	4SrSDC	2.48×10^{-3}	0.21	2.00×10^{-2}	4.38
4.	0.08 & 0.06	6SrSDC	3.60×10^{-3}	0.15	1.47×10^{-2}	4.14

In the present study, replacement of Sm^{3+} by Sr^{2+} in $Ce_{0.80}Sm_{0.20}O_{1.90}$ causes four opposite effects. According to Yamamura et al. (2000) co-doping suppresses the ordering of oxygen vacancies and consequently increases the configurational entropy. This leads to decrease in the activation energy of conduction and hence enhance the conductivity. The number of associated defect $[Sm'_{Ce}\text{-}V_O^{\bullet\bullet}]^{\bullet}$ pairs decreases as twice the number of Sr^{2+} ions added. This decreases total number of associated defect pairs leading to enhancement of the ionic conductivity. According to Kim et al. (1989) a large lattice mismatch between the host and dopant cations produces strain in the lattice. It decreases the conductivity due to increase in the activation energy. The lattice mismatch between Sr^{2+} 1.26 Á) and Ce^{4+} (0.97 Á) is more than that between Sm^{3+} (1.079 Á) and Ce^{4+} (0.97 Á).

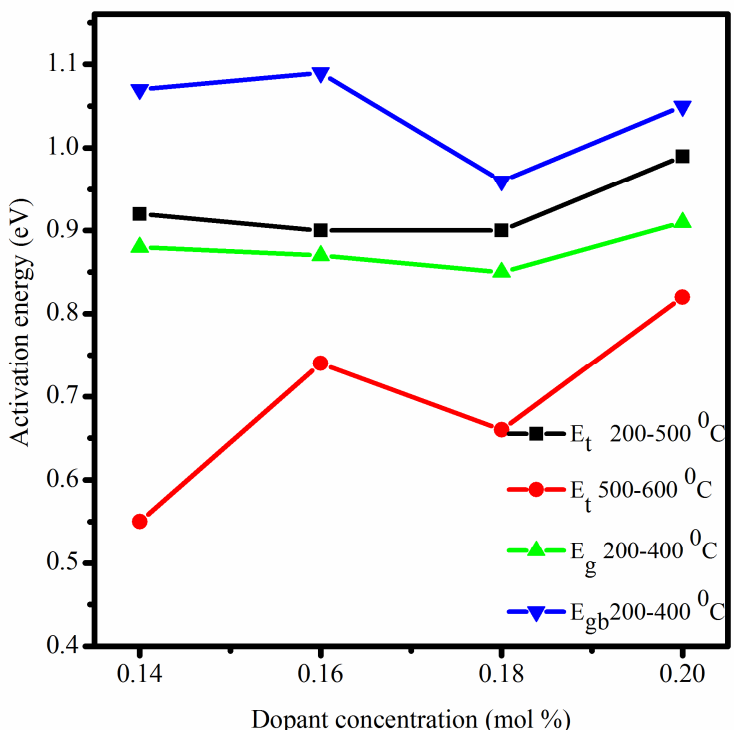

Fig. 6.11 Plots of variation of activation energy with dopant concentration for $Ce_{1-x-y}Sm_xSr_yO_{1.90}$ system

This causes an increase in the association enthalpy of the dopant-vacancy pairs [Sr''_{Ce}-$V_O^{\bullet\bullet}$]$^{\times}$ due to elastic strain [Butler et al. (1983); Kilner (1983)] and hence the activation energy increases and conductivity decreases. The first two factors dominate up to $y \leq 0.02$ and the last two factors starts dominating for $y > 0.02$. Sr^{2+} content up to 2 mol% seems to be an optimum value for molar concentration of Sr^{2+} which gives the maximum conductivity. Ionic conductivity increases also due to scavenging effect of strontium. Since conductivity of the composition, $Ce_{0.82}Sm_{0.16}Sr_{0.02}O_{1.90}$ is comparable to the highest conductivity reported for some electrolytes as mentioned above, use of this material as a solid electrolyte for IT-SOFCs will reduce the cost.

6.1.3 Conclusion

- Nanocrystalline co-doped ceria samples in the system $Ce_{1-x-y}Sm_xSr_yO_{1.90}$ where (x= 0.20, y=0), (x=0.16, y=0.02), (x=0.12, y=0.04) and (x=0.08, y=0.06) have been synthesized successfully using citrate nitrate route.
- Single phase solid solution of cubic fluorite structure has formed in all the samples.
- More than 95% of theoretical density has been achieved after sintering at 1350 ^oC.
- Radius of oxygen vacancies formed due to doping of Sm^{3+} and Sr^{2+} in ceria is found to be different in the system, $Ce_{1-x-y}Sm_xSr_yO_{1.90}$.
- Conductivity of the grain boundaries of co-doped samples increases due to scavenging effect of strontium.
- The composition $Ce_{0.82}Sm_{0.16}Sr_{0.02}O_{1.90}$ shows the highest ionic conductivity among all the samples.
- This makes it a potential candidate as a solid electrolyte for IT-SOFCs being much cheaper than ceria doped singly with Sm.

6.2 Nanocomposites of Sm and Sr Co-Doped Ceria (2SrSDC)

6.2.1 Introduction

Recently, research interests have been focused to decrease the operating temperature of SOFCs below 600 ºC [Yang et al. (2003); Goodenough (2000); Li et al. (2007); Huang et al. (2008)]. Problem with ceria based electrolytes is that Ce^{4+} gets reduced to Ce^{3+} in reducing atmosphere. This increases the electronic conduction which leads to short circuiting of the cell. In the recent years, a series of functional dual phase ceria/salts nanocomposites have been explored to reduce the electronic conduction and enhance the ionic conductivity [Zhu (2003); Zhu (2011); Huang et al. (2007); Huang et al. (2005)]. A typical ceria/salts composite is ceria/carbonates composite system, e.g. $Ce_{0.80}Sm_{0.20}O_{1.90}/Li_2CO_3$-$Na_2CO_3$ (SDC-LNCO) often containing one molten phase at the fuel cell operating temperature.

Among the composite materials, $Ce_{0.80}Sm_{0.20}O_{1.90}/Li_2CO_3$-$Na_2CO_3$ composites have been widely used as electrolytes for LT-SOFCs. Their use shows excellent power density between 400 and 600 ºC [Huang et al. (2005); Wang et al. (2008); Zhang et al. (2009)]. Therefore, by combining two approaches viz co-doping and nanocomposite idea, further increases the conductivity at low temperatures [Raza et al. (2010)]. In the above given results (section 1) for the system, $Ce_{1-x-y}Sm_xSr_yO_{1.90,}$ the composition 2SrSDC (x=0.16, y=0.02) has the maximum ionic conductivity in the series. Nanocomposites of 2SrSDC with binary mixture of Li_2CO_3-Na_2CO_3 abbreviated as SSDC/LNCO have been prepared and characterized.

6.2.2 Results and Discussion

(a) Thermal analysis

Fig. 6.12 shows DTA plots of all the composites and pure carbonate eutectic mixture. Two endothermic peaks have been found in the DTA plots. One is observed around 100 ºC. This may be due to loss of adsorbed moisture. Second endothermic peak is ascribed to the melting of the binary carbonate mixture.

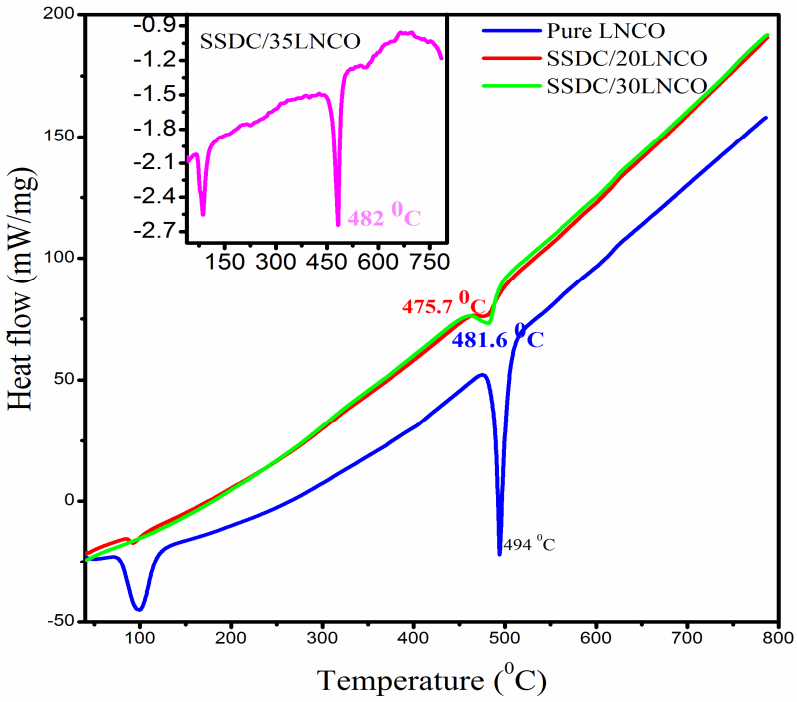

Fig. 6.12 DTA plots of all the samples in the system SSDC/LNCO

The second endothermic peak is observed at 475.7, 481.6, 482 ºC for the compositions containing 20, 30 and 35 wt% of carbonates respectively. It is noted from Fig. 6.12 that in the composite electrolytes, second endothermic peak appears at temperature lower than the melting temperature of the pure carbonates (494 ºC). It is known that melting point of a solid phase decreases as its average particle size becomes smaller. When the carbonate content is small, then it is dispersed uniformly in the SSDC phase. With increasing carbonate content, agglomeration occurs leading to increase in the melting point.

(b) Crystal structure and phase

Powder XRD patterns of all the milled (uncalcined), calcined and sintered samples are recorded. All the peaks are indexed on the basis of cubic fluorite structure of CeO_2 (JCPDS File no. 43-1002).

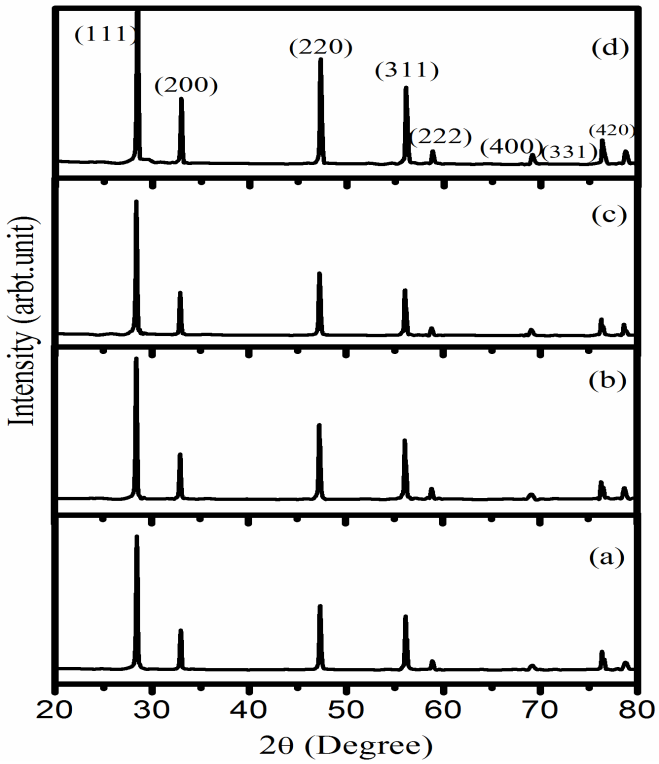

Fig. 6.13 Powder X-ray diffraction patterns of the sintered samples of compositions (a) Pure LNCO (b) SSDC (c) SSDC/20 LNCO (d) SSDC/30 LNCO (e) SSDC/35 LNCO

Fig. 6.13 shows XRD patterns of all the sintered samples of SSDC/LNCO nanocomposites along with SSDC. All the compositions have been found to be single phase. There is no peak of carbonates even when the content of carbonate is 35 wt%. This implies that carbonates exist as an amorphous phase in the composite. XRD patterns of the milled powders are the same as that of the calcined and sintered samples except that peaks are broad in the case of milled samples. Average crystallite size, D, of the milled composite powders (uncalcined) determined by Scherrer's formula is in the range of 14-16 nm.

Density of the sintered pellets is found to be ~82% of the theoretical value. This is due to low sintering temperature (700 ºC). These composites, however, can still be used as electrolytes because carbonates melt at the working temperature. Then, it fills in the pores and serves as seals to avoid crossover of gases [Huang et al. (2006)].

c) Microstructure

SEM micrographs of SSDC and the composite samples are shown in Fig. 6.14 (i)-(iv). Micrograph of SSDC shows a dense structure and well defined grains separated by the grain boundaries. It can be seen from Figs. 6.14 (ii) - (iv) that the SSDC particles are surrounded by carbonate phase. SEM micrographs of nanocomposites reveal that the size of SSDC particles is less than 100 nm and these have spherical shape. Due to presence of large pores between ceria grains, percolation of the carbonate phase is obvious. These micrographs show that interface between SSDC and LNCO provides more paths for ionic conduction. EDS spectrum of the composition SSDC/35LNCO at two different points is shown in Fig. 6.15. All the constituent elements are present in the spectrum as per stoichiometry except Li. It is seen from the EDS spectra that both the ceria and carbonate phases are distributed homogeneously.

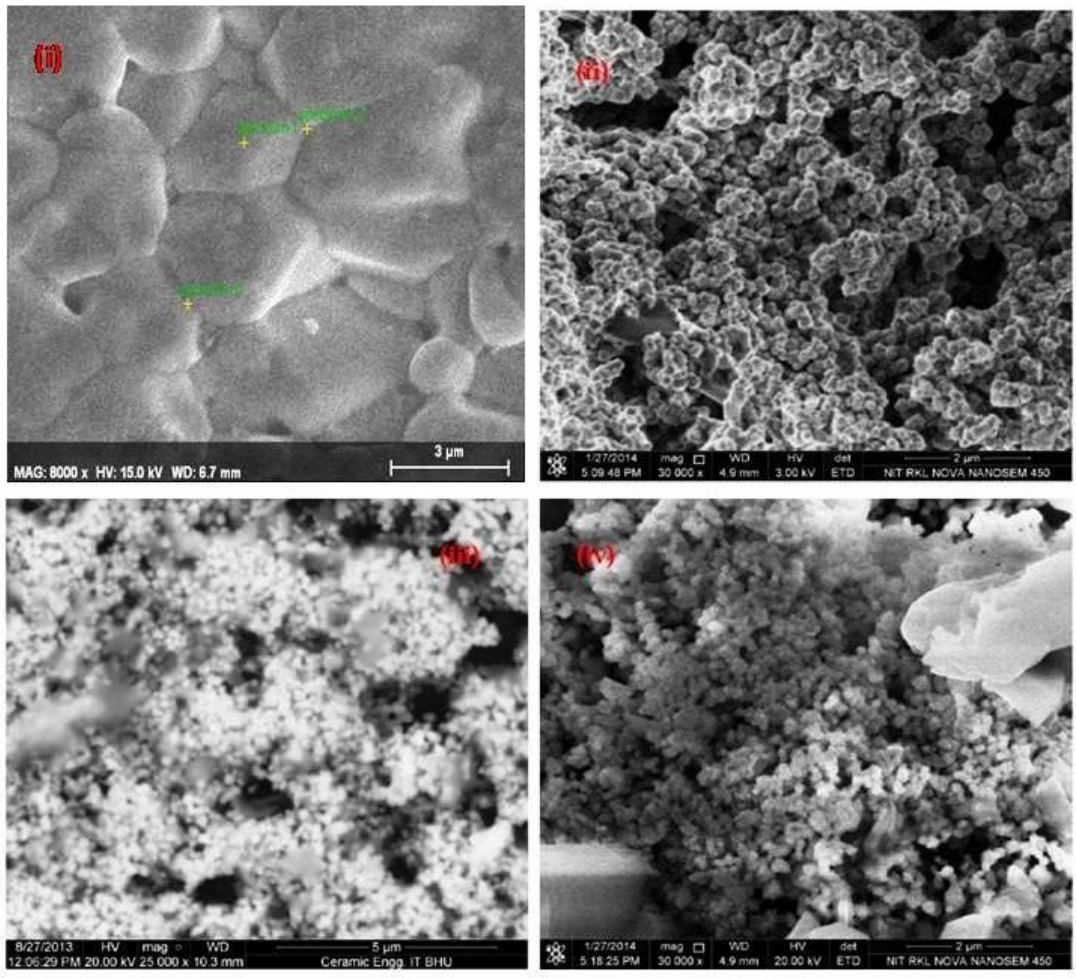

Fig. 6.14 SEM micrographs of the sintered samples of compositions (i) SSDC (ii) SSDC/20 LNCO (iii) SSDC/30 LNCO (iv) SSDC/35 LNCO

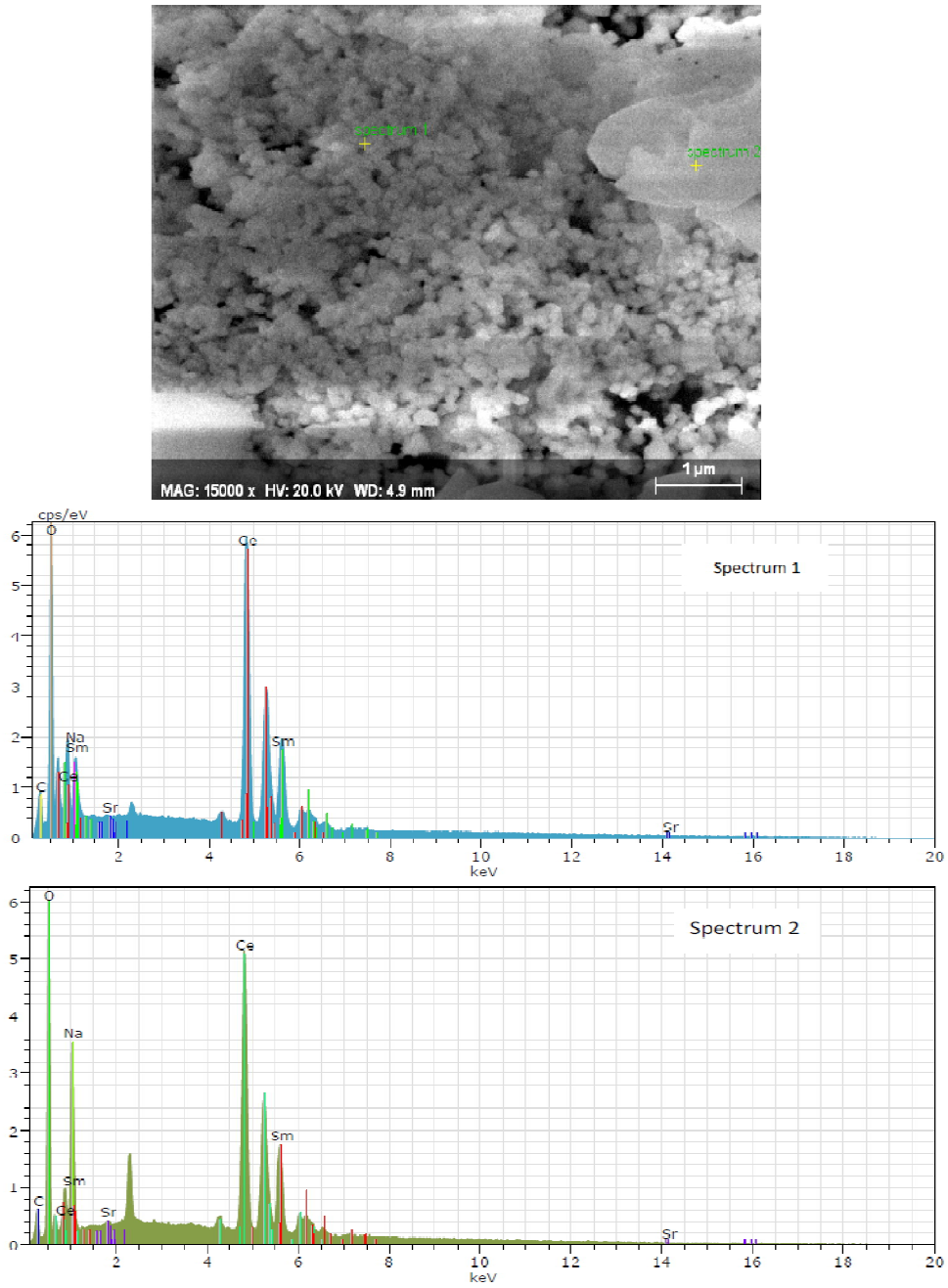

Fig. 6.15 EDS of the composition SSDC/35LNCO at two different points

(d) Thermal expansion

Fig. 6.16 shows plots of thermal expansion of all the nanocomposites. All the plots show linear behavior up to a particular temperature.

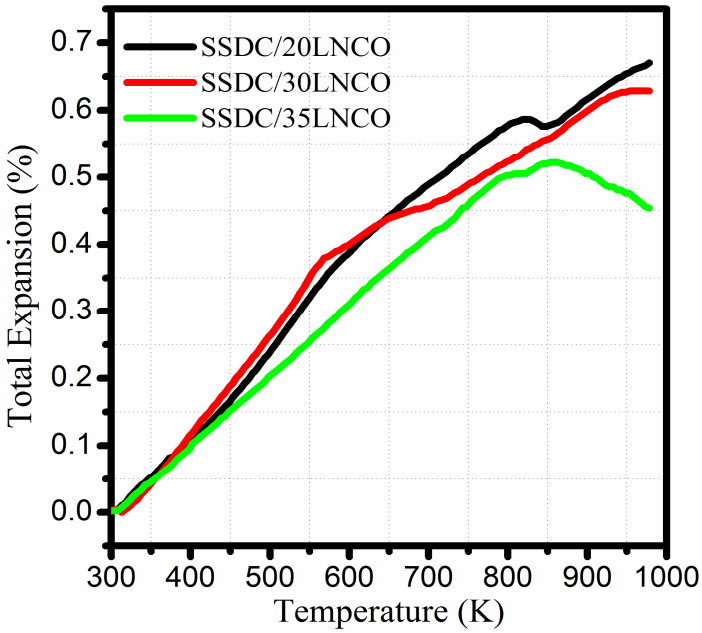

Fig. 6.16 Thermal expansion curves for SSDC/LNCO nanocomposites

Deviation from the linearity occurs above a certain temperature. It corresponds to the softening of the carbonates. The temperature of deviation is different in the different samples.

Table. 6.4 Values of CTE for all the composite samples

S. No.	Compositions	CTE ($\times 10^{-6}$ K^{-1})
1.	SSDC/20LNCO	11.80
2.	SSDC/30LNCO	12.00
3.	SSDC/35LNCO	13.00

Average thermal expansion coefficient (CTE) of all the samples in the temperature range 303-973 K is given in Table. 6.4. Values of CTE increase slightly with increasing the carbonate content.

(e) Electrical conductivity

Complex plane impedance plots of all the compositions are shown in Figs. 6.17-6.19 at different temperatures. In the case of composition, SSDC/20LNCO, two depressed

circular arcs along with a tail at lower frequency has been observed in the temperature range 200-250 ^{o}C. The arc passing from the origin is ascribed to the contribution of the grains. The arc in the intermediate frequency range corresponds to the contribution of the grain boundaries. A tail in the low frequency range is ascribed to the contribution of the electrode/electrolyte interface polarization. Relaxation frequency of all the polarization processes increases with increasing temperature. This leads to shifting of the arcs toward higher frequency. The arcs due to the grains and the grain boundaries, therefore, are not observed at higher temperatures. The arc of the grains and the grain boundaries disappear above 250 and 300 ^{o}C respectively. Only the arc due to electrode/specimen interface is observed at temperature > 300 ^{o}C. The grains and grain boundaries arcs are associated with the capacitances in the pF (10^{-10}-10^{-12}) and nF (10^{-7}-10^{-9}) ranges respectively. It is determined from the relationship $2\pi f_{max}RC = 1$, where f_{max} is the frequency at the highest point of the arc, R is the resistance and C is the capacitance of a particular contribution [Hodge et al. (1976)].

Above 450 °C, a tail starts appearing on the lower frequency side of the electrode arc. This is ascribed to a mass transfer process [Di et al. (2010)]. It has been clear from this distinct phenomenon that the conduction mechanism in the composite electrolytes is different from the single phase doped ceria electrolytes. The arc of the electrode is large because of the barrier between the ionic conduction in the electrolyte and the electronic conduction in the electrode [Zhu (2003)]. Similar behavior has been observed for the compositions SSDC/30LNCO and SSDC/35LNCO.

The impedance plots are fitted to an equivalent circuit as shown in the Figs. 6.17-6.19. The sum of resistance of the grains and the grain boundaries is equal to the total resistance of the sample. Therefore, only arcs of the grains and grain boundaries are fitted. The arc of the electrode is not fitted. At temperature > 325 °C, the total resistance is determined from the intercept on the high frequency side of the electrode arc on the real axis (Z').

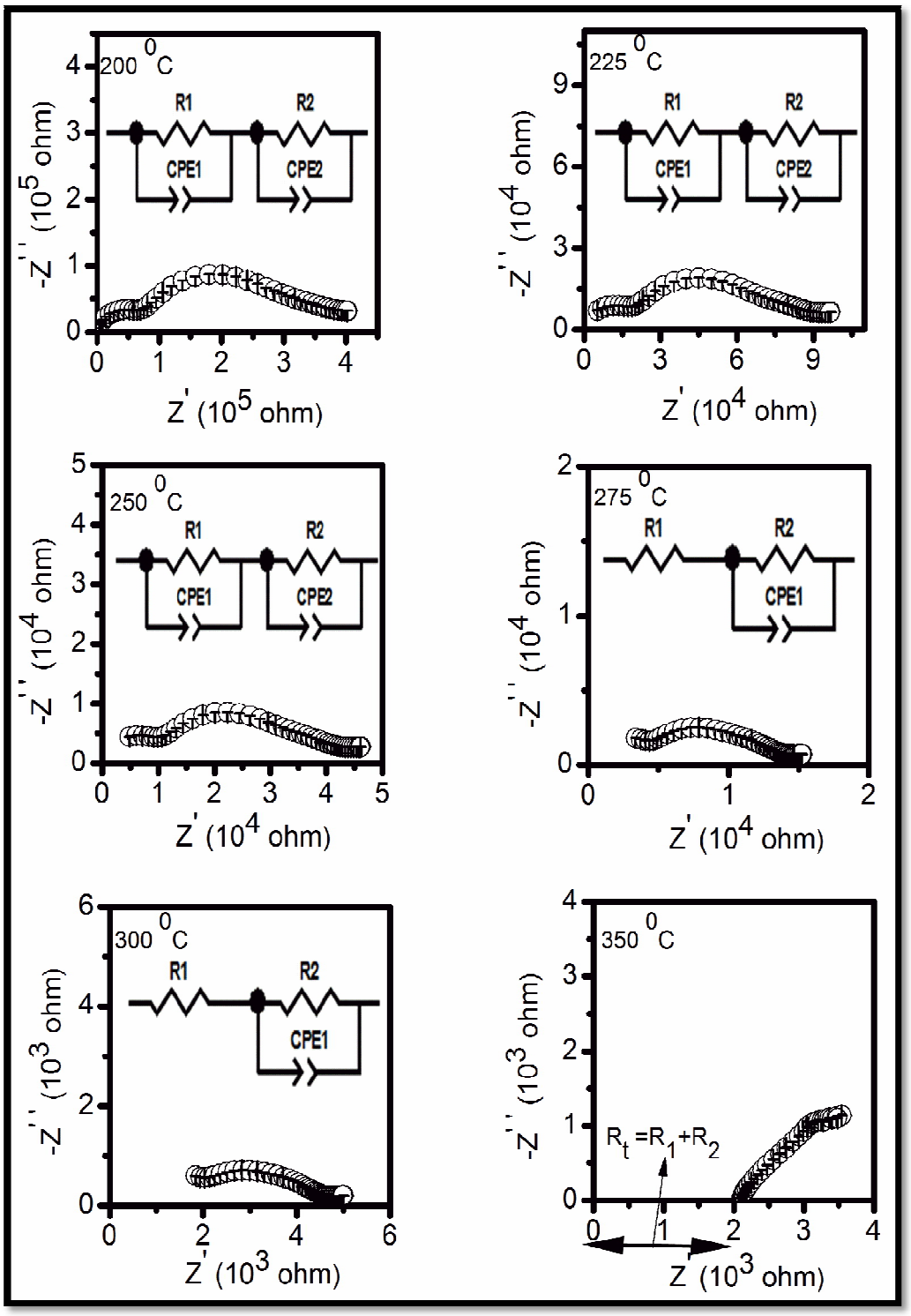

Fig. 6.17 Complex plane impedance plots of the composition SSDC/20LNCO at different temperatures

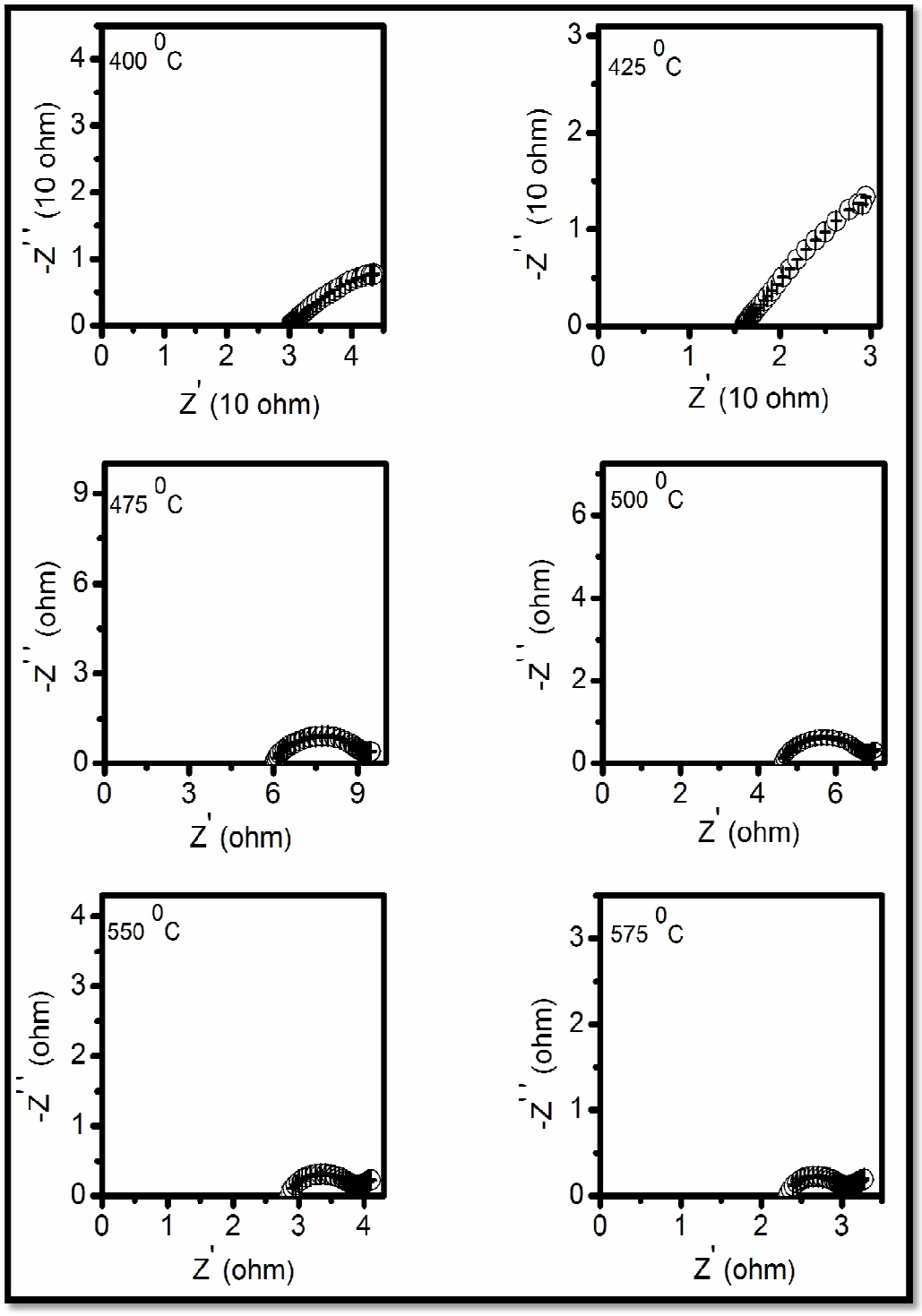

Fig. 6.17 Complex plane impedance plots of the composition SSDC/20LNCO at different temperatures

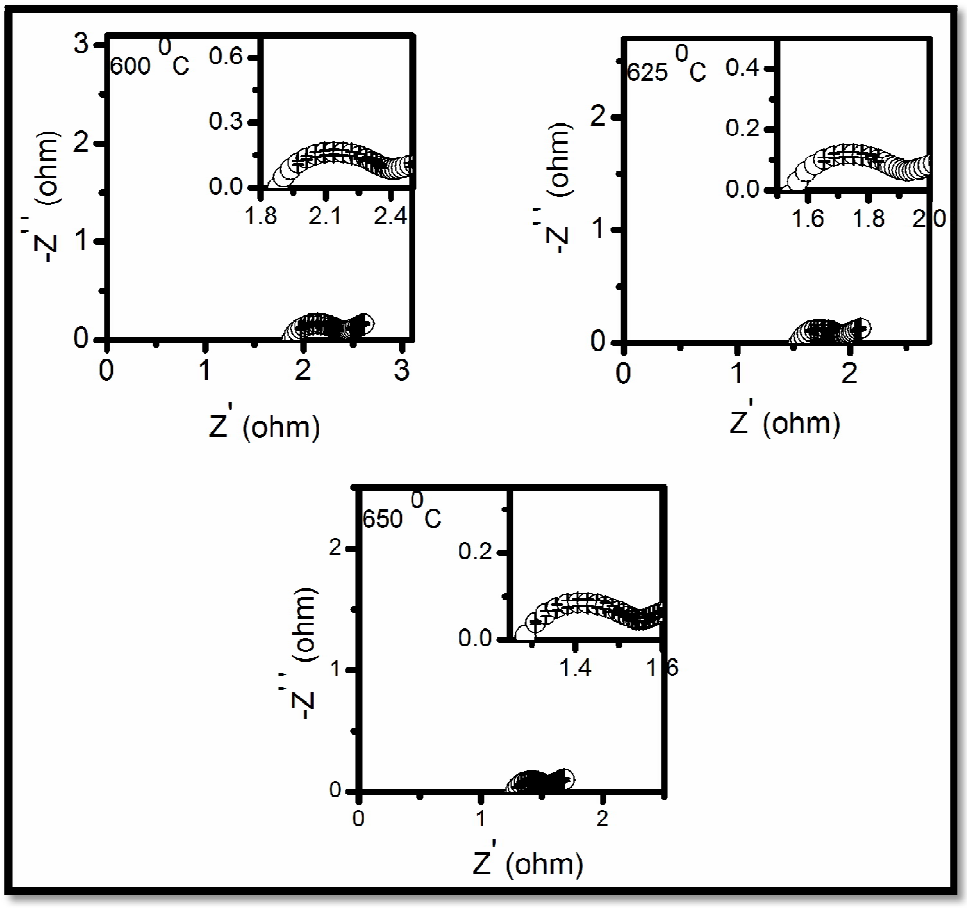

Fig. 6.17 Complex plane impedance plots of the composition SSDC/20LNCO at different temperatures

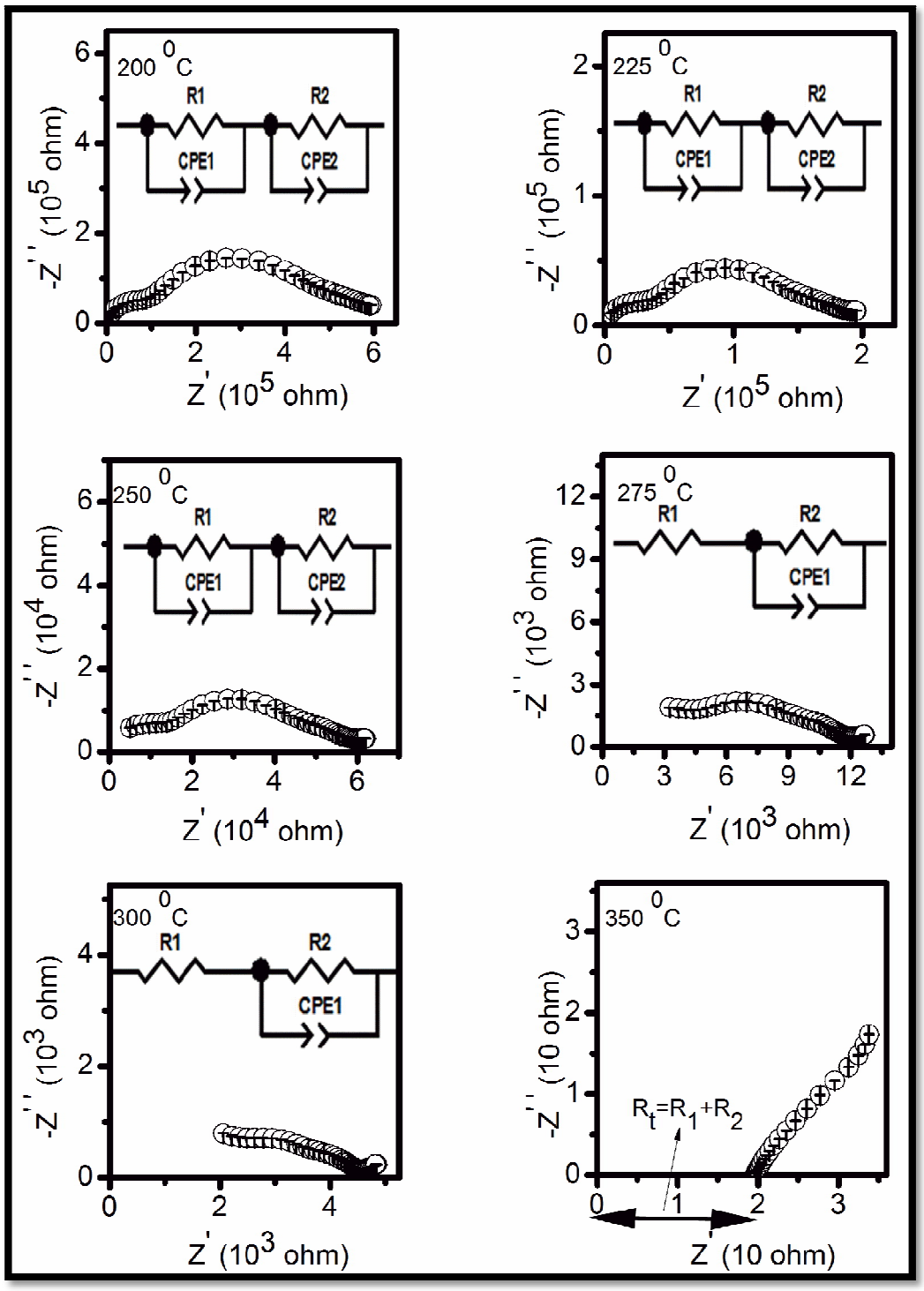

Fig. 6.18 Complex plane impedance plots of the composition SSDC/30LNCO at different temperatures

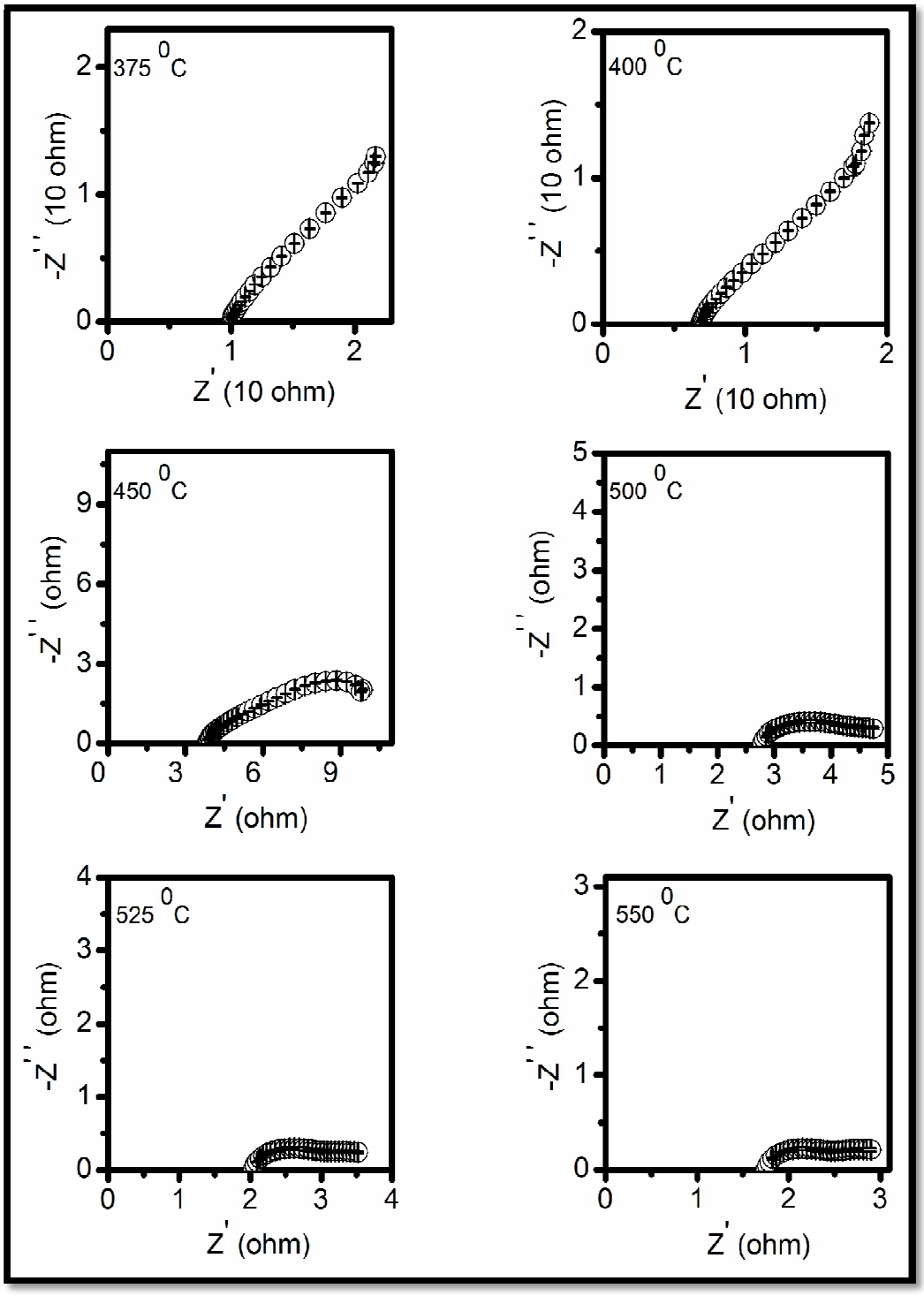

Fig. 6.18 Complex plane impedance plots of the composition SSDC/30LNCO at different temperatures

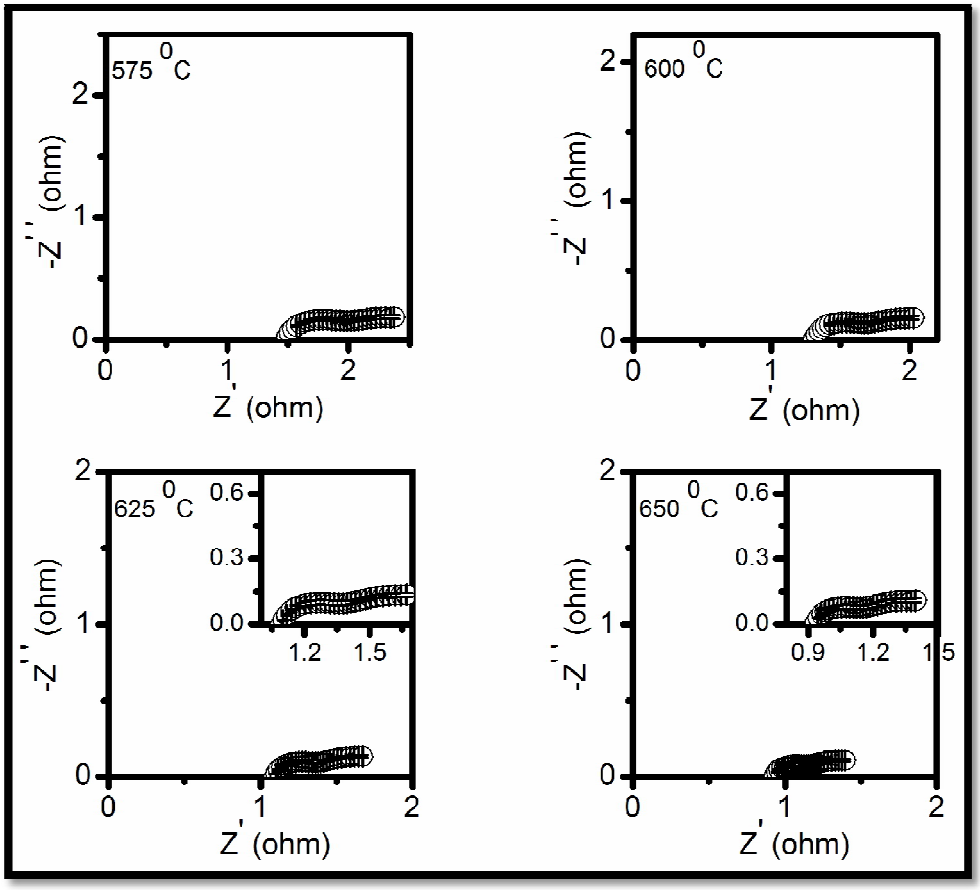

Fig. 6.18 Complex plane impedance plots of the composition SSDC/30LNCO at different temperatures

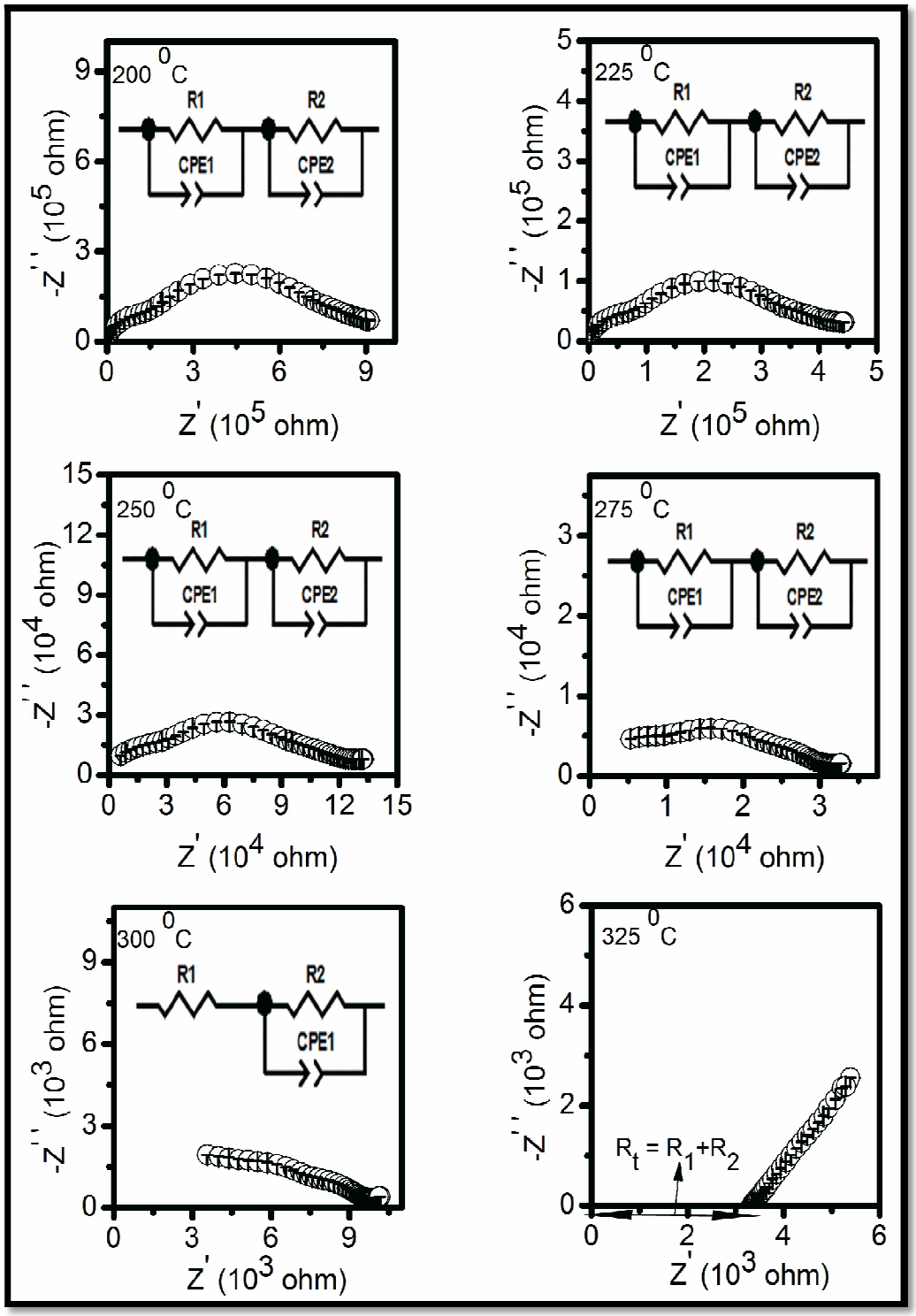

Fig. 6.19 Complex plane impedance plots of the composition SSDC/35LNCO at different temperatures

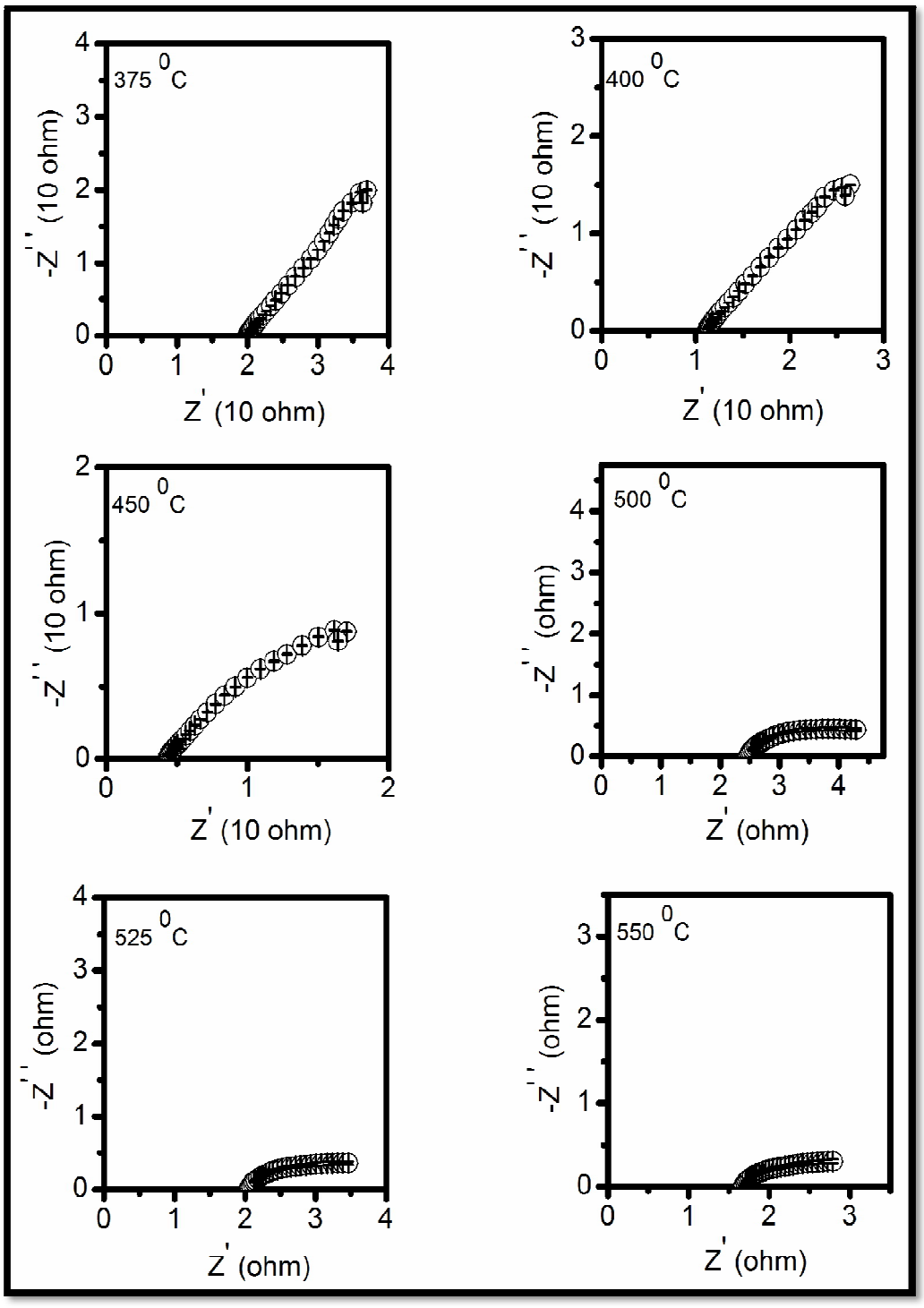

Fig. 6.19 Complex plane impedance plots of the composition SSDC/35LNCO at different temperatures

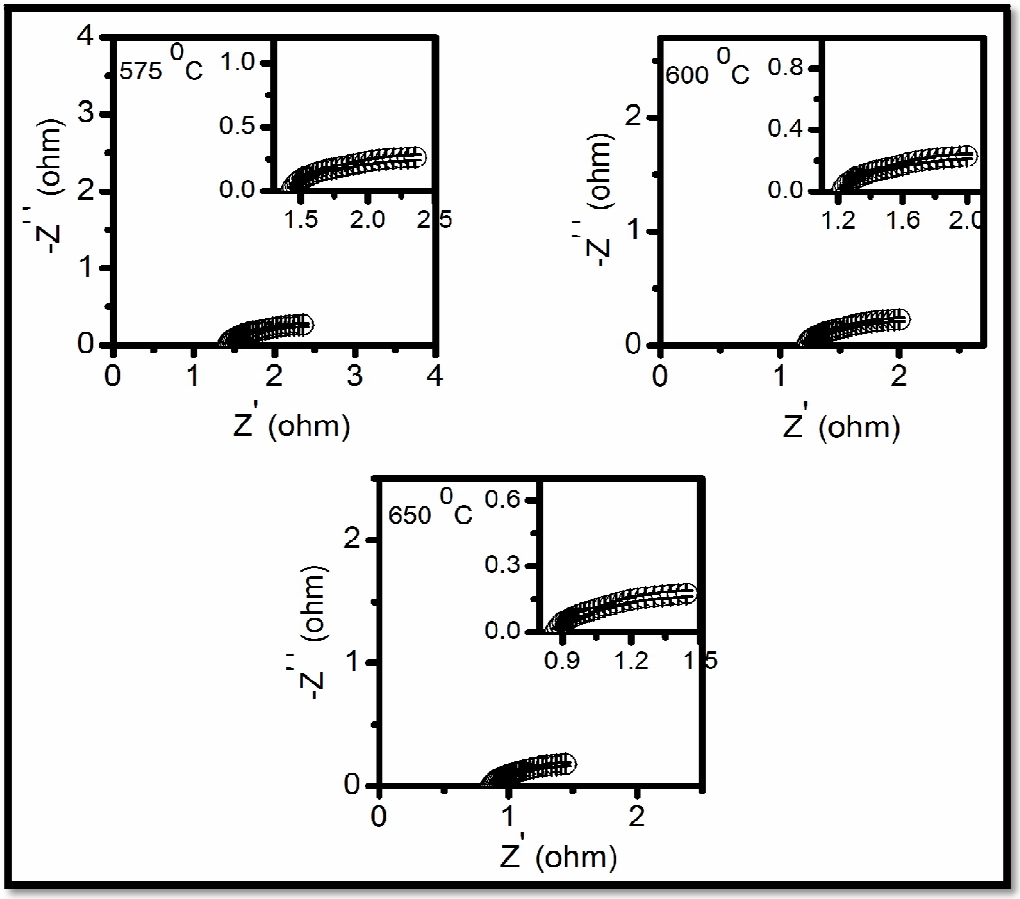

Fig. 6.19 Complex plane impedance plots of the composition SSDC/35LNCO at different temperatures

Fig. 6.20 shows Arrhenius plots for the total ionic conductivity of all the composites along with the compositions SSDC and pure LNCO mixture. Arrhenius plots have an elongated z-shape curves and a jump in the conductivity is observed in all the composites. This behavior is distinct from that of SSDC. It is noted from the Fig. 6.20 that the transition temperature is not coinciding with the melting temperature of carbonates even preceding this temperature. It increases with increasing the carbonate content. The transition temperatures for the composites containing 20, 30 and 35 wt% of carbonates are 350, 350 and 375 ºC respectively.

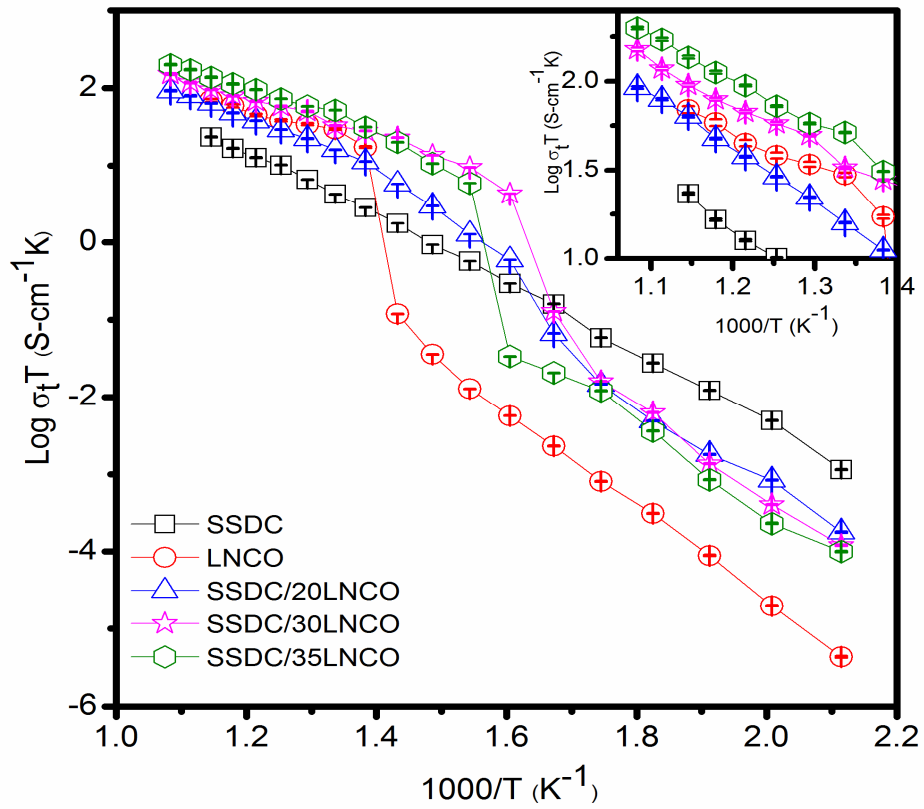

Fig. 6.20 Arrhenius plots of all the compositions in the system SSDC/LNCO

Variation of transition temperature with the carbonate content is explained as a result of percolation threshold to form highly conducting continuous path at the interfaces [Huang et al. (2007)]. Lowering of transition temperature is the cause of interaction between the ceria and carbonate phases.

Enhancement in the conductivity has been interpreted as a superionic phase transition at the interfaces formed between the ceria and carbonate phases. Superionic transition in the composites is determined by the interfaces, i.e. a process that breaks symmetry of the matrix by introducing a structural discontinuity [Ying et al. (2012)]. Above the transition point, conductivity of the composite electrolytes is more than that of SSDC and pure LNCO. In the nanocomposites, O^{2-} ions conduct through the interfaces and in the bulk of SSDC. Due to melting from the sublattice to the bulk, Li^{+}, Na^{+} and CO_3^{2-} ions also contribute to the conduction.

All the composites show more conductivity than the pure carbonate (LNCO) above the transition point except the composition, SSDC/20LNCO. Composition, SSDC/20LNCO has conductivity one order of magnitude more than that of SSDC and ~50% less than that of LNCO. This may be due to less area of interface region as compared to the compositions containing higher concentration of carbonates. Values of the conductivity of all the compositions are given in Table. 6.5.

Activation energy of conduction (E_a) and pre-exponential factor (σ_0) have been determined by fitting the data points to Arrhenius equation. Values of E_a and σ_0 for all the samples are given in Table. 6.5. Activation energy obtained in the case of SSDC/35LNCO is less (0.48 eV) than that of pure SSDC (0.67 eV) at temperature >400 ºC. At lower temperatures, activation energy is ~1.10 eV. It is due to blocking of O^{2-} ions by dispersed solid carbonates below the transition temperature. Composites have high value of σ_0 i.e. higher concentration of mobile defects than that in SSDC and LNCO.

Table. 6.5 Total conductivity at 500 ºC, pre-exponential factor (σ_0) and activation energy at temperature >400 ºC for all the compositions

S. No.	Composition	σ_t at 500 °C S/cm	σ_0	E_a for T > 400 °C (eV)
1.	SSDC	8.46×10^{-3}	3.18×10^{6}	0.68
2.	LNCO	4.73×10^{-2}	3.05×10^{6}	0.30
3.	SSDC/20LNCO	2.87×10^{-2}	3.14×10^{8}	0.67
4.	SSDC/30LNCO	5.23×10^{-2}	1.40×10^{9}	0.53
5.	SSDC/35LNCO	7.48×10^{-2}	8.99×10^{9}	0.48

The composition, SSDC/35LNCO exhibits the highest ionic conductivity of all the compositions. This is due to three reasons: (i) partial substitution of Sm^{3+} and Sr^{2+} in ceria enhances the conductivity as discussed in section 1 (ii) the large interface region between the ceria and the carbonate phase leads to superionic conduction and (iii)

increase in the value of σ_0 i.e. increase in the number of mobile ions and long jump distance at the interfaces. Variation of conductivity with the carbonates content is explained by the percolation model [Delnick et al. (1990); Stauffer (1985)] and it is expressed in the form of Archie equation (as discussed in Chapter 4). Archie plot of the system SSDC/LNCO is shown in Fig. 6.21.

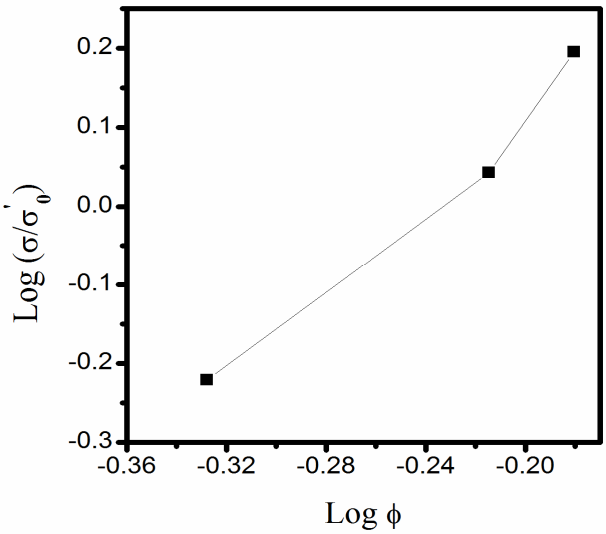

Fig. 6.21 Archie plot for SSDC/LNCO system

It is seen from Fig. 6.21 that the composition dependence of electrical conductivity of SSDC/LNCO system deviates from the linearity and slightly bends towards lower normalized conductivity. In the present work, the conductivity of SSDC/35LNCO electrolyte attains a value as high as 0.068 S/cm at 475 °C which is one order of magnitude higher than the value 5.64×10^{-3} S/cm for SSDC at the same temperature. This value is also higher than the value 0.01 S/cm at 481 °C reported for $Ce_{0.8}Sm_{0.1}Nd_{0.1}O_{1.9}/(Li/Na)_2CO_3$ by Liu et al. (2010). It is concluded that the interaction between two the phases may essentially lead to more paths for diffusion of the ions resulting in superionic conduction.

6.2.3 Conclusion

- In the present work, nanocomposites of SSDC/LNCO with varying amount of carbonates have been prepared successfully.
- Single phase solid solution (SSDC) has formed in all the samples. This shows that no reaction occurs between the ceria and the carbonate phases.
- It has been observed that the conductivity changes rapidly at a particular temperature which is below the melting point of the carbonates. This is called as superionic transition at the interfaces.
- Above the transition point, composites show high ionic conductivity with low activation energy of conduction.
- Conductivity of the composition, SSDC/35LNCO is the maximum of all the compositions being 7.48×10^{-2} S/cm at 500 °C.
- Use of this composition as solid electrolyte for LT-SOFCs will reduce the cost as compared to that of $Ce_{0.8}Sm_{0.1}Nd_{0.1}O_{1.9}/(Li/Na)_2CO_3$ or $Ce_{0.80}Sm_{0.20}O_{1.90}$/LNCO.